Universidade de Aveiro
2017

Departamento de Engenharia de Materiais e Cerâmica

Kiryl Zakharchuk

Defect chemistry of pyrochlore-type $(Gd,Ca)_2(Ti,Mo)_2O_7$ for prospective electrocatalytic applications

Química de defeitos de materiais $(Gd,Ca)_2(Ti,Mo)_2O_7$ de tipo pirocloro para aplicações electrocatalíticas

Universidade de Aveiro
2017

Departamento de Engenharia de Materiais e Cerâmica

Kiryl Zakharchuk

Defect chemistry of pyrochlore-type $(Gd,Ca)_2(Ti,Mo)_2O_7$ for prospective electrocatalytic applications

Química de defeitos de materiais $(Gd,Ca)_2(Ti,Mo)_2O_7$ de tipo pirocloro para aplicações electrocatalíticas

Dissertação apresentada à Universidade de Aveiro para cumprimento dos requisitos necessários à obtenção do grau de Mestre em Engenharia de Materiais, realizada sob a orientação científica do Doutor Aleksey Yaremchenko, Investigador Principal do Departamento de Engenharia de Materiais e Cerâmica da Universidade de Aveiro, e do Doutor Jorge Ribeiro Frade, Professor Catedrático do Departamento de Engenharia de Materiais e Cerâmica da Universidade de Aveiro.

o júri

Presidente

Professor Doutor Joaquim Manuel Vieira

Professor Catedrático do Departamento de Engenharia de Materiais e Cerâmica da Universidade de Aveiro

Vogais

Doutor Aleksey Yaremchenko

Investigador Principal do Departamento de Engenharia de Materiais e Cerâmica da Universidade de Aveiro

(Orientador)

Doutor João Carlos de Castro Abrantes

Professor Adjunto, Instituto Politécnico de Viana do Castelo

(Arguente)

acknowledgements

I would like to express my gratitude to my supervisors Dr. Aleksey Yaremchenko and Prof. Jorge Frade for teaching and for help in experimental work during the last years.

Additional many thanks to my previous supervisors Dr. E. Naumovich, Dr. A. Kavaleuski, and to my colleague from the Belarus State University - Ekaterina Kravchenko – for the collaboration.

palavras-chave

Pirocloros, pilhas de combustível de eletrólito sólido, ânodo, química de defeitos, condutividade mista, condutividade protónica, expansão térmica

resumo

O principal objetivo deste trabalho foi a caracterização de soluções sólidas derivadas do pirocloro $Gd_2Ti_2O_7$ com co-substituições de Gd e Ti por Ca e Mo, respetivamente, para eventuais aplicações electrocatalíticas. O trabalho foi motivado por desvantagens dos ânodos cermetos de Ni-YSZ propostos para pilhas de combustível, designadamente degradação microestrutural, intolerância a alterações redox, contaminação com enxofre e deposição de carvão. Os pirocloros à base de $Gd_2Ti_2O_7$ foram considerados adequados para o desenvolvimento de componentes para ânodos alternativos, por co-substituições em ambas as posições catiónicas, sem degradação da estrutura do pirocloro, conferindo condução mista e atividade electrocatalítica,.

Em condições oxidantes, a gama de soluções sólidas de $(Gd_{1-x}Ca_x)_2(Ti_{1-y}Mo_y)_2O_{7\pm\delta}$ com estrutura de pirocloro situa-se entre $0.10 < x < 0.15$ e $0.05 < y < 0.10$, sendo as amostras cerâmicas da composição $(Gd_{1-x}Ca_x)_2(Ti_{0.95}Mo_{0.05})_2O_{7\pm\delta}$ estáveis numa vasta gama de pressão parcial de oxigénio, sem degradação detetável por difração de Raios-X, termogravimetria ou comportamento elétrico. Materiais à base de $Gd_2Ti_2O_7$ com co-substituições possuem coeficiente de expansão térmica linear de $(10.5\text{-}10.7)\times10^{-6}$ K^{-1} a 25-1100℃, em ar, e estabilidade dimensional com variações redox, sendo quase nula a expansão química até $p(O_2) \sim 10^{-12}$ atm, a 950℃.

Os mecanismos de compensação e transportadores de carga predominantes em condições oxidantes dependem da razão Ca:Mo. Co-substituição por molibdénio suprime a condutividade iónica e origina mudança de condução predominantemente iónica para eletrónica ou mista.

Observou-se aumento de condutividades iónica e eletrónica com decréscimo na pressão parcial de oxigénio, conferindo condutividade mista a cerâmicos de $(Gd,Ca)_2(Ti,Mo)_2O_{7-\delta}$ em condições típicas de operação dos ânodos. Foi desenvolvido um modelo de química de defeitos que descreve as variações de propriedades elétricas em função das condições redox e co-substituições. Além disso, relacionou-se a condutividade protónica a mais baixas temperaturas, em atmosferas húmidas, com a concentração de lacunas de oxigénio na rede do pirocloro, tendo a humidade um forte impacto na resistividade das fronteiras de grão.

keywords

Pyrochlore, solid oxide fuel cell, anode, defect chemistry, mixed conductivity, ionic conductivity, protonic conductivity, thermal expansion

abstract

The main objective of the work was design and comprehensive characterization of solid solutions derived from pyrochlore-type $Gd_2Ti_2O_7$ by co-substitutions of Gd and Ti by Ca and Mo, respectively, for prospective electrocatalytic applications. The work was motivated by the disadvantages of commonly used cermet Ni-YSZ cermet anodes including long-term microstructural degradation and intolerance to redox changes, sulfur poisoning and carbon deposition. Pyrochlore-type $Gd_2Ti_2O_7$ was considered as a suitable parent material for the development of alternative mixed-conducting ceramic components for SOFC anodes, while simultaneous co-substitutions of both host cations are likely to allow flexible tuning of transport and redox properties of Mo-containing pyrochlores, with impact on electrocatalytic activity, while preserving phase stability provided by pyrochlore-type titanate lattice.

The range of $(Gd_{1-x}Ca_x)_2(Ti_{1-y}Mo_y)_2O_{7\pm\delta}$ solid solutions with cubic pyrochlore-type structure was found to be limited to $0.10 < x < 0.15$ and $0.05 < y < 0.10$ under oxidizing conditions. $(Gd_{1-x}Ca_x)_2(Ti_{0.95}Mo_{0.05})_2O_{7\pm\delta}$ ceramics demonstrate good phase stability in a wide range of oxygen partial pressures with no degradation or phase decomposition evidenced in the course of electrical and thermogravimetric studies and by subsequent XRD. Co-substituted $Gd_2Ti_2O_7$-based ceramics possess moderate thermal expansion coefficients compatible with solid electrolytes, $(10.5\text{-}10.7)\times10^{-6}$ K^{-1} at 25-1100℃ in air, and demonstrate remarkable dimensional stability with nearly zero chemical expansion down to $p(O_2) \sim 10^{-12}$ atm at 950℃.

Dopant compensation mechanism and type of dominating charge carriers under oxidizing conditions is demonstrated to be strongly dependent on calcium/molybdenum ratio. Co-substitution by molybdenum suppresses ionic conduction and results in a change from dominating ionic to prevailing electronic or mixed ionic-electronic transport. Reducing oxygen partial pressure increases both ionic and n-type electronic conductivities, and $(Gd,Ca)_2(Ti,Mo)_2O_{7-\delta}$ ceramics exhibit mixed conductivity under SOFC anode operation conditions. Defect chemistry model is developed to describe variations of electrical properties in co-substituted materials. Low-temperature protonic transport in $Gd_2Ti_2O_7$-based titanates in wet atmospheres was found to correlate with concentration of oxygen vacancies in the pyrochlore lattice, with stronger impact of humidity on the grain boundary resistivity.

Table of contents

List of figures

List of tables

Abbreviations

EDS	– energy dispersive X-ray spectroscopy
EMF	– electromotive force
JCPDS PDF	– powder diffraction file of Joint Committee on Powder Diffraction Standards
MIEC	– mixed ionic-electronic conductor
Ni/YSZ	– composite of metallic Ni and yttria-stabilized zirconia ceramic
PEMFC	– proton exchange membrane fuel cells
SEM	– scanning electron microscopy
SOFC	– solid oxide fuel cell
TEC	– thermal expansion coefficient
TGA	– thermogravimetric analysis
XPS	– X-ray photoelectron spectroscopy
XRD	– X-ray diffraction
YSZ/8YSZ	– yttria-stabilized zirconia / 8 mol% Y_2O_3 fully stabilized ZrO_2

List of symbols

A_0 – pre-exponential factor

AC – alternating current

C_b – capacitance of grains bulk

C_{gb} – capacitance of grain boundaries

CPE – constant-phase-element

e – elementary charge, $1.602 \cdot 10^{-19}$C

E_a – activation energy

F – Faraday constant, $9.6485\ 10^4$ C·mol^{-1}

k_0 – constant of valence changes between molybdenum cations Mo^{5+}/ Mo^{4+}

k_1 – constant of valence changes between molybdenum cations Mo^{6+}/ Mo^{5+}

k_{aF} – anti-Frenkel disorder constant

k_e – constant of electronic defects formation

k_{red} – reduction constant

L – length of sample

n – concentration of electrons

p – concentration of holes

$p(H_2O)$ – partial pressure of water vapor

pO_2 – partial pressure of oxygen

R – gas constant, 8.304 J·mol^{-1}·K^{-1}

R_b – resistance of grains bulk

R_e – polarization resistance of electrode

R_{gb} – resistance of grain boundaries

$r^N_{A^{n+}}$ – ionic radii of cation A^{n+} with coordination number N

S – cross-sectional area of sample

T – temperature

t_e – electronic transference number

t_H – protonic transference number

t_O – oxygen-ion transference number

X – atomic coordinate of oxygen ion in 48f site

Z' – real part of impedance

Z'' – imaginary part of impedance

α – thermal expansion coefficients

$\Delta\delta$ – change of oxygen nonstoichiometry

μ – charge carriers mobility

μ_n – mobility of electrons

μ_{pol} – mobility of polarons

μ_V – mobility of oxygen vacancies

σ – conductivity

σ_e – electronic conductivity

σ_O – oxygen-ionic conductivity

σ_{pol} – polaron hopping conductivity

ω – current frequency

Ø – diameter of sample

Introduction

Electrochemical devices for energy conversion, such as batteries and fuel cells, are becoming more common due to its high efficiency and lack of mechanical elements. Solid Oxide Fuel Cells (SOFC) is most prospective type of fuel cells for large scale electrical power generation. Unlike of other types of fuel cells, SOFC can operate not only with pure hydrogen but also with hydrocarbons - high operating temperature facilitates electrocatalytic decomposition of heavy organic molecules. This factor reduces the requirements for fuel quality, which is important in the case of industrial large-scale electricity production. On the other hand, high operation temperature limits application of SOFC as portable devices. Additional prospective application of high temperature electrochemical cells is electrocatalytic partial oxidation of hydrocarbons and biofuel for syngas production for subsequent use as a fuel in portable fuel cells or in chemical industry.

Up to date, commercial application of SOFC is still moderate due to limited lifetime and higher prices compared to conventional devices. The main problem is mechanical and chemical stability of components operating at high temperature. Currently used electrode materials have suitable properties for continuous operation during thousands of hours. However, heating/cooling and oxidation/reduction cycles lead to fast degradation of microstructure of multicomponent fuel cell assembly due to different thermal expansion coefficients (TEC) and chemical expansion of electrodes. Second problem is poisoning of anode with impurities in a fuel (such as sulfur) and precipitation of carbon when hydrocarbons (e.g. methane) are used as a fuel. Replacement of conventional anode, which is a composite made of metallic nickel and yttria stabilized zirconia (YSZ), by single-phase oxide material with high mixed ionic-electronic conductivity may help to overcome several problems at the same time: to enhance tolerance to sulphur, to reduce carbonization of surface and to avoid microcracking during heating/cooling cycles.

One strategy in development of advanced anode-membrane system is to use the same parent oxide material modified by doping to create prevailing ionic conductivity for membrane and mixed ionic-electronic conductivity for anode. One potential parent material is $Gd_2Ti_2O_7$ with pyrochlore structure [1]. This structure contains arranged vacant oxygen sites which facilitates diffusion of oxygen. Substitution of host cations by aliovalent cations may significantly increase oxygen-ionic conductivity and, in addition, may induce electronic conductivity [2, 3]. Main criteria for selection of substituting cation are oxidation states and ionic radii. Gadolinium and titanium ions in pyrochlore structure have significantly different ionic

radii (Gd^{3+} – 1.053Å, Ti^{4+} – 0.605 Å) and are arranged in two sublattices. This fact allows to separate their substitution by different types of cations for fine tuning of electrochemical properties. Based on previous and values of ionic radii, calcium and molybdenum were chosen as dopants for Gd and Ti sublattices, respectively. Lower oxidation state of Ca^{2+} in Gd^{3+} sites is expected to result in formation of oxygen vacancies and improvement of ionic conductivity. Multivalent Mo-cations in Ti sites should lead to formation of conduction electrons. In a case of partial oxidation of hydrocarbons, variable oxidation states of molybdenum may improve catalytic properties: Mo^{6+}/Mo^{5+} redox couple is known to facilitate oxidation of chemisorbed organic molecules [4, p.34].

The present work focused on the synthesis and characterization of $(Gd,Ca)_2(Ti,Mo)_2O_7$ solid solutions: phase relationships, stability under reducing conditions, ionic and electronic transport, defect chemistry, and thermomechanical properties. Several factors turn these pyrochlores, moderately co-substituted by Ca and Mo, into possible candidates for anode components. These include mixed ionic-electronic conductivity under reducing conditions, chemical compatibility and similar thermal expansion coefficients with YSZ membranes [5], phase stability under reducing conditions. As was discovered during this work, total conductivity is rather moderate for application in SOFC, but electrocatalytic activity of molybdenum and tolerance to carbonization make it prospective for use in devices for partial oxidation of hydrocarbons and biofuel.

Chapter 1. State of the art and objectives

1.1. Solid oxide fuel cells – an overview

Fuel cells are electrochemical devices for direct electrical power generation via oxidation of fuel - hydrocarbons or hydrogen. There are many types of fuel cells based on materials with selective ionic conductivity: H^+, O^{2-}, OH^-, CO_3^{2-} (Table 1). Each of them has its own technical characteristic including operating temperature, type of fuel, power range, and type of application (portable or stationary devices). General advantages of all types of fuel cells in comparison with chemical-mechanical devices for fuel/energy conversion are:

- High energy conversion efficiency (40-70%) due to direct electrical power generation. For example, conversion efficiency of a system with diesel engine and electrical generator is only about 30-40%.
- Coefficient of performance is not so much dependent on the load than that of machines based on the Carnot cycle.
- Absence of heavily loaded mechanical devices and, as a consequence, absence of the noise/vibrations.
- Tolerance to overload.
- High fuel efficiency reduces impact on environment. In case of hydrogen fuel there are no pollutant emissions, only water as exhaust.

Table 1. Types of Fuel Cells and their applications [6].

Fuel cell	*Electrolyte*	*Anode fuel*	*Cathode gas*	*T(°C)*	*Applications*
Alkaline fuel cell (AFC)	KOH solution	H_2	O_2	60–90	Spacecraft, submarines
Proton exchange membrane fuel cell (PEMFC)	Proton conductive polymer membrane	H_2	O_2 (in air)	60–90	Transportation vehicles, stationary power plants, cogeneration plants, portable power supplies
Direct methanol fuel cell (DMFC)	Proton conductive polymer membrane	Methanol	O_2 (in air)	90–120	Transportation vehicles, stationary power plants, cogeneration plants, portable power supplies
Phosphoric acid fuel cell (PAFC)	Phosphoric acid	H_2	O_2 (in air)	200	Stationary power plants, cogeneration plants
Molten carbonate fuel cell (MCFC)	Molten alkaline carbonate	H_2, CH_4, or coal gas	O_2 (in air)	650	Stationary power plants, cogeneration plants
Solid oxide fuel cell (SOFC)	Ceramic solid electrolyte	H_2, natural gas, coal gas	O_2 (in air)	800–1000	Stationary power plants, cogeneration plants

Solid oxide fuel cells can work with larger variety of fuels in contrast with other types of fuel cells since high operating temperature reduces potential barrier of hydrocarbons decomposition and oxidation. High temperature provides a number of specific advantages:

- High kinetic energy of molecules facilitates the decomposition and dissociation of organic substances on electrodes;
- Increased rate of surface exchange processes between membrane, electrodes and gas phase;
- Relatively cheap materials are used as electrodes instead of platinum while preserving electrocatalytic activity and stability. For instance, low temperature PEMFC can operates only with platinum catalyst on electrodes due to very low catalytic activity of alternative materials at low temperatures, and this problem is far from being solved;
- Relatively low electrode polarization under high load and high current densities due to fast gas diffusion in porous electrodes and high mobility of ions. In other words – rapid diffusion of gases and oxygen ions in membrane reduces concentration polarization and overall losses;
- No catalyst poisoning by carbon monoxide;
- Possibility of chemical co-generation: electrocatalytic conversion of hydrocarbons and biofuels via partial oxidation and reforming into low molecular weight chemicals (liquid fuels, syngas).

At the same time, high working temperature limits application areas of SOFCs: heating to operating temperature takes a lot of time and energy. It is preferable to produce stationary devices with high output power (>1kW) working in continuous mode. Generally, high costs of SOFC production and limitations of lifetime are related to:

- chemical degradation of components due to interdiffusion of cations;
- microstructural degradation under heating/cooling cycles and due to chemical expansion;
- poisoning and deactivation of Ni-containing anode with sulphur;
- high cost of materials of fuel cells – membrane, electrodes, stack materials (special chromium-containing steels for interconnects);
- complexity of production of thin-layered membranes free of mechanical defects.

1.2. Principles of operation

Scheme of hydrogen SOFC with electrode reactions presented in Fig. 1. The electrodes are porous materials with mixed ionic-electronic conductivity, and membrane is usually made yttria-stabilized zirconia (YSZ) – a pure oxygen-ionic conductor. These materials should be stable under corresponding operating conditions - reducing for anode and oxidizing for cathode. The anode is usually made of zirconia-based cermet – a composite of zirconia and metallic

nickel (Ni/YSZ). The cathode is usually metal oxides with perovskite structure and mixed ionic-electronic conductivity, for example (La,Sr)MnO_3. Operation temperature of state-of-the-art SOFC is 800-1000°C. The ionic conductivity of yttria-stabilized zirconia is provided by oxygen vacancies: $Y_2O_3 \xrightarrow{ZrO_2} 2Y'_{Zr} + V_O^{\bullet\bullet} + 3O_O^x$. Value of specific ionic conductivity is 0.02 - 0.1 S/cm at operating temperatures and it is comparable to that of liquid electrolytes. Thickness of YSZ membrane can be very small – 15-50 μm to avoid ohmic loss. Interconnect materials usually are alloys chemically stable at high temperatures or ceramics with expansion coefficients close to that of YSZ to avoid mechanical stress, for instance (La,Sr)CrO_3. The hermetization or sealing of the cells is achieved using glasses or glass/ceramic composites that have transition temperature close to the operating temperature of the cell. A main problem of using glasses for sealing is the migration of silica from glasses to electrodes causing degradation in cell performance.

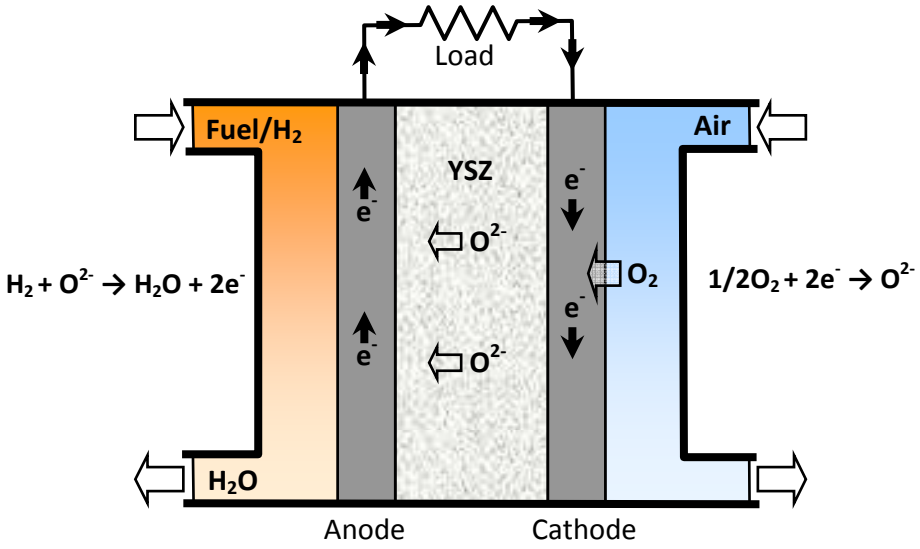

Fig. 1. Scheme of hydrogen SOFC.

Theoretical potential without load and with hydrogen as fuel can be calculated by Nernst equation (1). In realistic conditions, open circuit voltage is in a range 1.0-1.2V; the value may vary depending on the type of fuel and the oxygen partial pressure difference across membrane.

$$E_{cell} = E_{cell}^0 + \frac{RT}{2F} \ln\left(\frac{pH_2 \cdot (pO_2)^{1/2}}{pH_2O}\right) \quad (1)$$

E - the electromotive force (or reversible open circuit voltage)

E_{cell}^0 - standard Nernst potential at 1 atm and 25°C

R - the universal gas constant

F - Faraday constant

p_i - partial pressure

Under load, the voltage of fuel cell is reduced due to overpotential. Typical current-voltage curve of fuel cells is represented on Fig. 2. The sources of overpotential are polarization effects of different nature. There are three main mechanisms of polarizations:

- Activation polarization is related to overcoming of activation energy of electrochemical reactions on electrodes. High temperature and electrocatalytic activity of electrodes reduces impact of this polarization in overall value of overpotential.
- Ohmic losses - resistivity of all components of fuel cell. Usually have linear dependence on the current in accordance with Ohm's law.
- Concentration polarization begins to be important at high current densities due to limited rates of diffusion of gaseous reactants to the surface of porous electrodes and removal of reaction products.

Each mechanism has different impact on the total voltage drop depending on the current density, kinetics of surface exchange reactions on electrodes, catalytic activity and level of ionic-electronic conductivity of each component. Voltage drop can de calculated by equation (2).

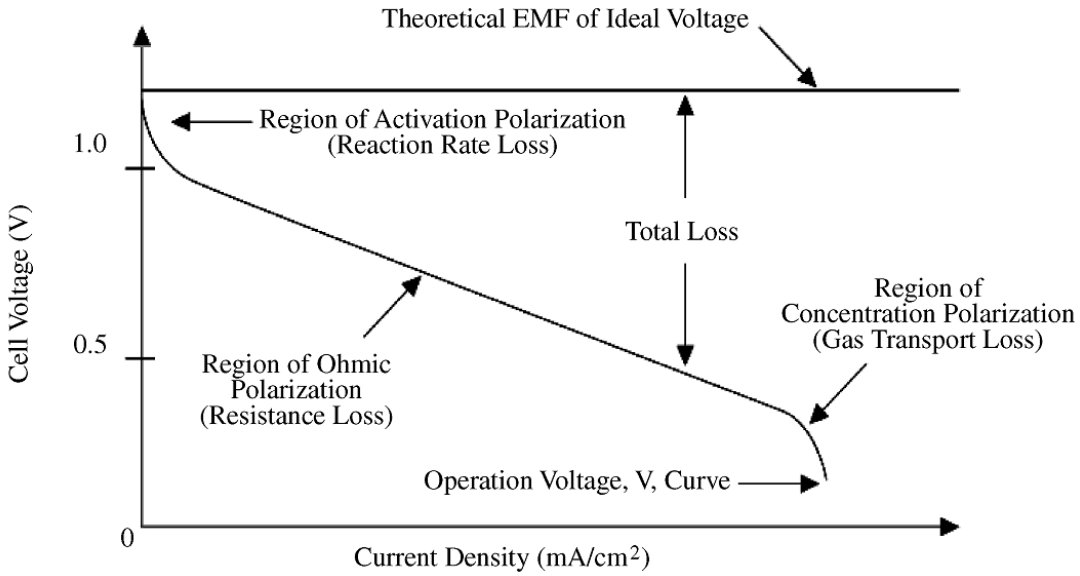

Fig. 2. Typical fuel cell current-voltage curve [7, p. 36].

$$V = E_0 - \Delta V_{ohm} - \Delta V_{act} - \Delta V_{transp} \quad (2)$$

V - cell voltage

E_0 - theoretical potential

ΔV - polarization losses

Selection of operating temperature of fuel cell is determined by the factors with opposite effects on price and performance. Increase in temperature increases the rates of diffusion of gaseous chemicals to surface, ionic conductivity of membrane, facilitates dissociation of

chemicals and rate of surface exchange. All these lead to increase of power density. On the other hand, low operating temperature (700-800°C) requires lower amount of energy to maintain the working temperature, reduces degradation and the requirements for insulation / heat recovery of the reaction products.

Example of dependencies of voltage and power density versus current density and temperature for a real SOFC is shown on Fig. 3 (prototype of SOFC in NASA Glenn Research Center). These data clearly shows that optimum operating voltage is in a range 0.5-0.8 V near the maximum of power density; polarization effects at higher currents reduce voltage below adequate values. Combination of multiple cells in one stack with consistent electrical circuit allows producing electric power with desired voltage from single unit. Temperature range can be chosen only by taking into account many exploitation aspects, such as, stability of components, economical reasons etc. In recent years there is a tendency to reduce operating temperatures at 700-750°C and development of materials with advanced properties in this temperature range. Background of this tendency is reducing exploitation cost and degradation of components.

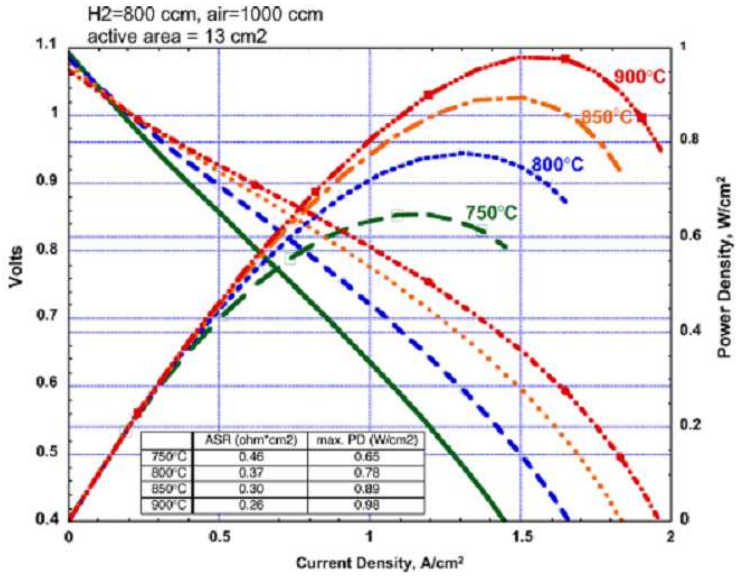

Fig. 3. Voltage and power density as function of current density of SOFC [8].

1.3. Common SOFC materials and disadvantages of Ni-YSZ anodes

The ceramics for high-temperature membranes with oxygen-ionic conductivity should be dense, gas-tight and high-purity to avoid electronic conductivity and internal leakage currents. The most used material for membranes is yttria-stabilized zirconia (8YSZ, 8 mol% of yttria) which is a pure oxygen-ion conductor in a wide range of oxygen partial pressure. Usually membranes have shape of thin sheets (up to 20µm) to reduce ohmic losses. Sintering of dense

thin sheets is a complex problem due to high sintering temperature and shrinkage. Most used technique for green body production is tape casting from slurry with following drying and sintering. Mechanical defects (cavities, cracks) cause leakages of gases and lead to inability to use. These requirements lead to comparatively high cost of production of membranes.

Electrode materials are porous ceramics with mixed ionic-electronic conductivity or cermet composites (anode) with high stability to oxidizing condition for cathode and reducing for anode. In general, development of electrode materials is the most complicated challenge in fuel cell technology due to the set of requirements. In addition to advanced electrochemical properties, electrodes must have:

- good adhesion to membrane to provide mechanical and electrical contact;
- thermal expansion coefficients similar to membrane;
- tolerance to contaminations in fuel (usually sulphur) to avoid poisoning and degradation.
- inertness in respect to membrane and current collectors, absence of interdiffusion of cations between membrane-electrodes-current collectors.

Most common materials of cathode are complex oxides with perovskite structure and high mixed conductivity. Besides commonly used (La,Sr)MnO_3, there is large variety of similar perovskites on the stage of development and research. Usual problem of cathode materials is reactions with current collector and membrane with formation of inert oxides: $La_2Zr_2O_7$ in case of YSZ-membrane and chromium-containing oxides on contacts with the current collector.

Usual composition of anode is porous mixture of nanosized particles of 40-50 vol% of metallic nickel with yttria-stabilized zirconia – 8YSZ = $(ZrO_2)_{0.92}(Y_2O_3)_{0.08}$. Nickel particles provide electronic conductivity under reducing conditions and catalytic properties, 8YSZ – oxygen-ionic conductivity. In total, composite have very good electrocatalytic activity for hydrogen oxidation and high ionic-electronic conductivity. At the same time, nickel in metal form is a cause of long-time degradation. There are several mechanisms of degradation. In the case of hydrocarbon fuels, this is the poisoning of nickel by sulphur (formation of NiS) and coking of metal particles (Fig. 4).

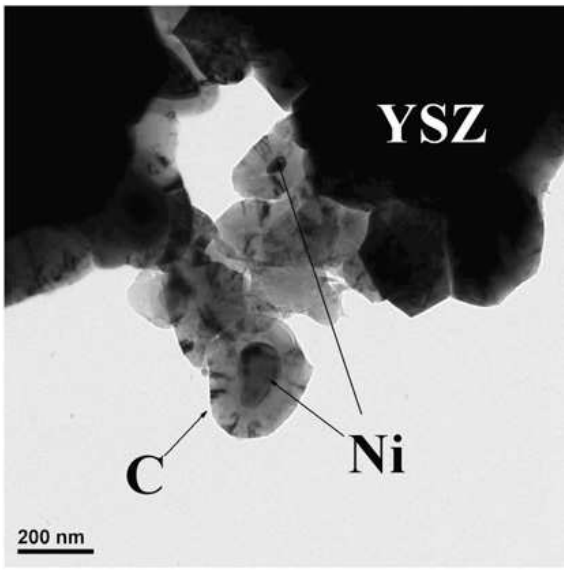

Fig. 4. Microstructure of coked Ni particles of anode [11].

Periodic oxidation of carbon on anode looks like obvious solution of problem, but oxidizing/reduction cycles causes microstructural degradation due to large dimensional changes - oxidation of nickel particles leads to significant change in the particle size and microcracking. As shown on Fig.5, several oxidizing/reduction cycles may leads to cracking of the entire anode-membrane-cathode assembly. This imposes restrictions on exploitation of fuel cells. Besides redox cycles, different TECs of components of electrochemical cell leads to an increase in mechanical stresses in case of stopping/starting of the fuel cell.

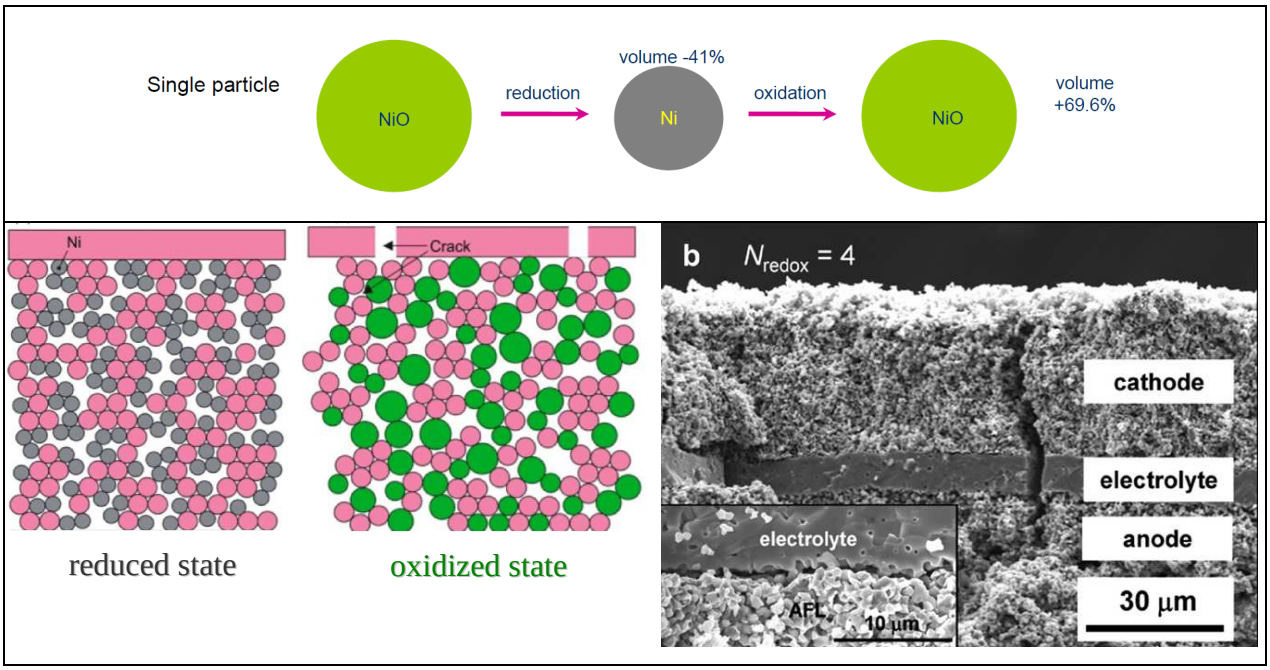

Fig.5. Schematic representation of microstructural degradation of Ni/YSZ composite during oxidizing/reduction cycles [10].

Even under constant working conditions with supply of pure hydrogen, there is mechanism of anode degradation - agglomeration and sintering of nickel particles during long operation at a high temperature (Fig. 6). This leads to a reduction in the specific area, losses of electrical connections between particles, degradation of conductivity and lowering of electrocatalitic activity.

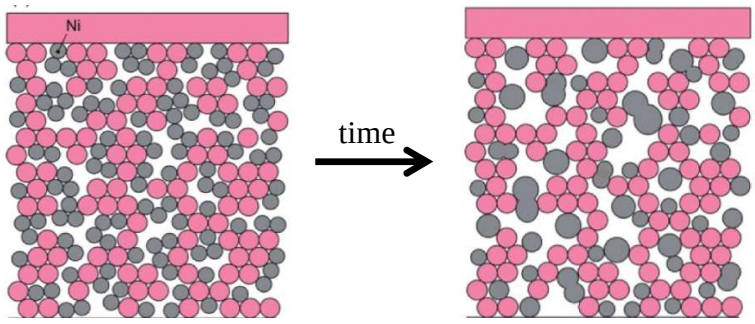

Fig. 6. Schematic representation of agglomeration/sintering of Ni particles with time.

Currently there are several trends in development of SOFC components. First is searching for materials with high performance at lower temperature (500-800°C), which will allow reducing the operating temperature. Second is development of electrodes more stable at high temperature with tolerance to sulphur. One approach to achieve compatibility between electrode and membrane is the use of the same parent material but doped with different cations.

Substitution generates different types of point defects providing ionic or mixed conductivity. One group of these parent materials can be oxides with pyrochlore-type structure, and the present work focused on doped gadolinium titanate. After substitution of host Gd/Ti cations by Ca and Mo, it potentially can be used as membrane material and as electrode material.

1.4. Prospective $Gd_2Ti_2O_7$-based anode materials

1.4.1. Overview of pyrochlore-type oxides

Pyrochlores are large group of complex oxides with general formula $A^{3+}{}_2B^{4+}{}_2O_7$ with cubic structure similar to fluorite and ordered oxygen vacancies. The possibility of formation of such structures can be described by using the concept of tolerance factor and is discussed in details in literature [11]. Oxygen vacancy concentration may differ from 1/8, and cubic structure might be distorted. Stability of pyrochlore phase depends on the ratio of ionic radii and oxidation states of A/B cations (Fig. 7). A^{3+} and B^{4+} cations have significant difference in ionic radii with approximate ratio ~1.6-1.75. The electrochemical properties of pyrochlore-type oxides at high temperature are diverse: $Ln_2Mo_2O_7$ is electronic conductor; $Gd_2Zr_2O_7$ and acceptor-doped $Ln_2Ti_2O_7$ are good ionic conductors. By selection of suitable cations and doping, it is possible to create materials with specified electrical and electrochemical properties.

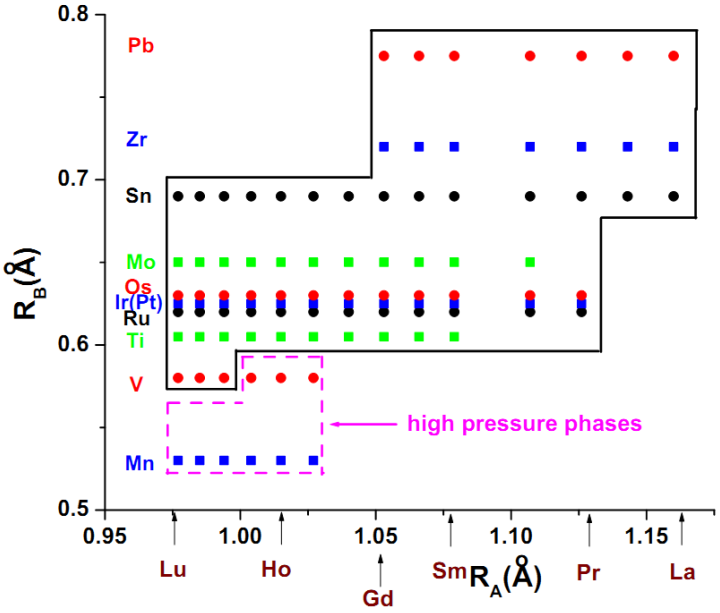

Fig. 7. Stability-field map for $A_2B_2O_7$ pyrochlores [12].

From the point of view of practical application in SOFC, the present work focused on the materials with highest ionic and mixed conductivity. According to the literature, $Gd_2Ti_2O_7$ is

suitable parent material for application as anode after acceptor- and donor- co-substitution to induce mixed conductivity [1,2]. Note, that pyrochlores with mixed conductivity may also have a contribution of protonic conductivity in wet atmospheres, as reported in some literature sources (Fig. 8) [13]. Impedance spectroscopy allows to detect the presence of protonic conductivity by comparison of impedance spectra measured in dry and wet gases.

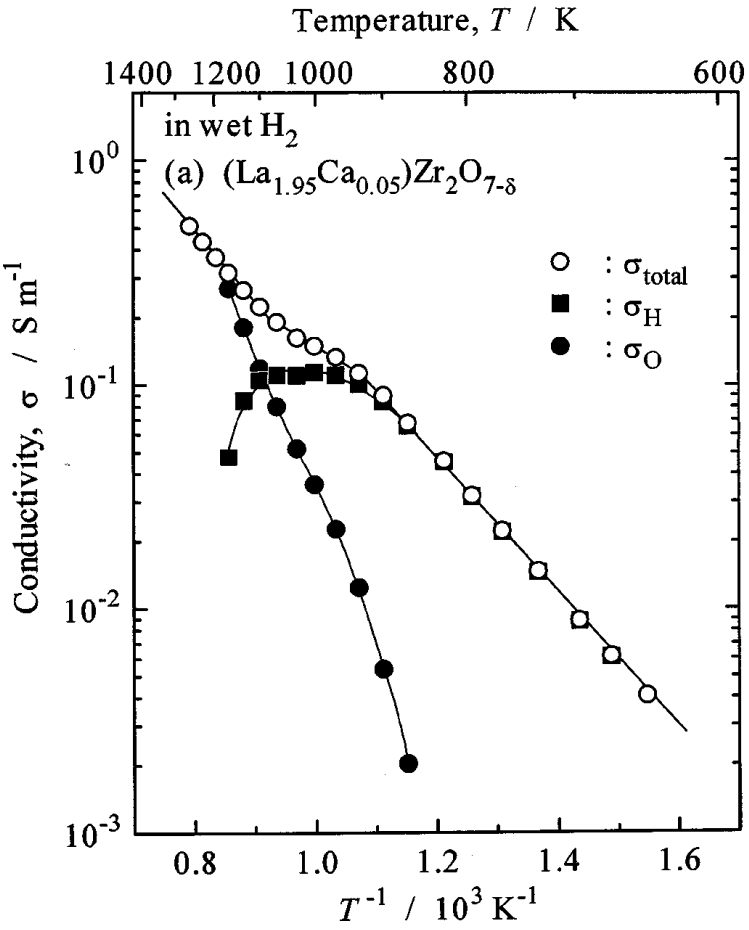

Fig. 8. Temperature dependence of partial oxygen-ionic (σ_O), electronic (σ_e) and protonic (σ_H) conductivities of $La_{1.95}Ca_{0.05}Zr_2O_{7-\delta}$ ceramics [13].

1.4.2. Crystal structure of $Gd_2Ti_2O_7$-based pyrochlores

The unit cell of $Gd_2Ti_2O_7$ can be described as a superstructure of 8 oxygen-deficient fluorite-type unit cells with 1/8 of oxygen sites remaining vacant. Oxygen sublattice is distorted from ideal fluorite. Oxygen vacancies are arranged in an ordered structure, and oxygen sublattice forms more complicated structure, so-called superstructure. Full unit cell and simplified 1/8 part are represented on Fig. 9. Crystallographic parameters and atomic coordinates are listed in Table 2. Due to the large difference in sizes of host cations, it is possible to differentiate the doping of

A and B sublattices. Similarity of atomic radii was one of the criteria for choosing of cations-substituents - Ca^{2+} and Mo^{6+} have radii close to Gd^{3+} and Ti^{4+}, respectively [14]:

$$r^{VIII}_{Gd^{3+}} = 1.053\,Å,\ r^{VIII}_{Ca^{2+}} = 1.12\,Å$$

$$r^{VI}_{Ti^{4+}} = 0.605\,Å,\ r^{VI}_{Mo^{6+}} = 0.59\,Å$$

Difference in oxidation state of dopants leads to formation of various point defects. Defect chemistry allows to predict electrical properties and phase stability, and modify it.

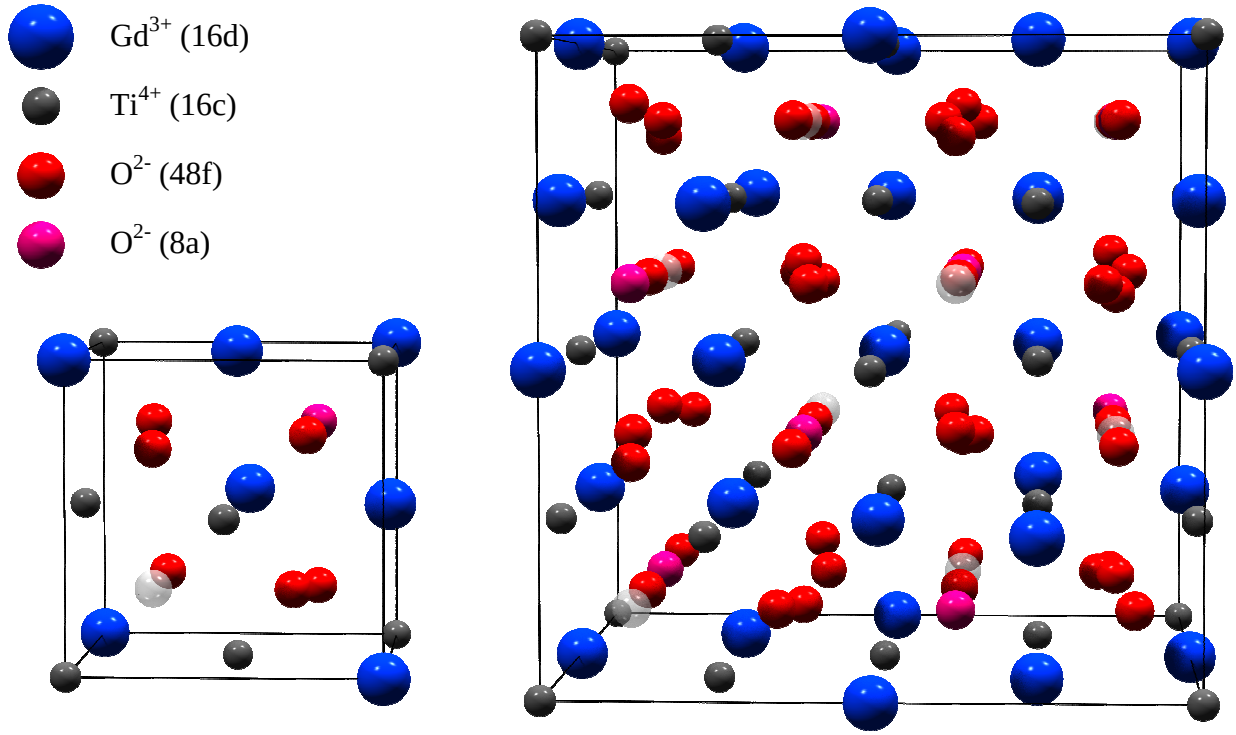

Fig. 9. Representation of $Gd_2Ti_2O_7$ pyrochlore-type structure. Semitransparent spheres are vacant O sites (representation created in Atoms and POV-Ray software).

Table 2. Atomic coordinates and crystallographic parameters of $Gd_2Ti_2O_7$ pyrochlore

	Wyckoff positions	Atomic coordinates	Symmetry
Gd^{3+}	16d	1/2, 1/2, 1/2	*F*d-3m (227)
Ti^{4+}	16c	0, 0, 0	
O^{2-}	48f	*X*, 1/8, 1/8 *(X ≈ 0.3125 — 0.375)*	a=b=c=10.2Å
	8a	3/8, 3/8, 3/8	α=β=γ=90°
Vacant sites	8b	1/8, 1/8, 1/8	

1.4.3. Ca- and Mo-substituted $Gd_2Ti_2O_7$

Undoped gadolinium titanate is an n-type semiconductor and has a low level of conductivity (σ_{total} ~10^{-5} S/cm at 900°C) (Fig. 10). Doping of $Gd_2Ti_2O_7$ by other elements may alter transport properties to significant extent. Partial substitution of Gd by Ca significantly improves oxygen-ionic conductivity, and $(Gd_{1-x}Ca_x)_2Ti_2O_7$ pyrochlores were proposed as potential electrolyte for solid oxide fuel cells [1].

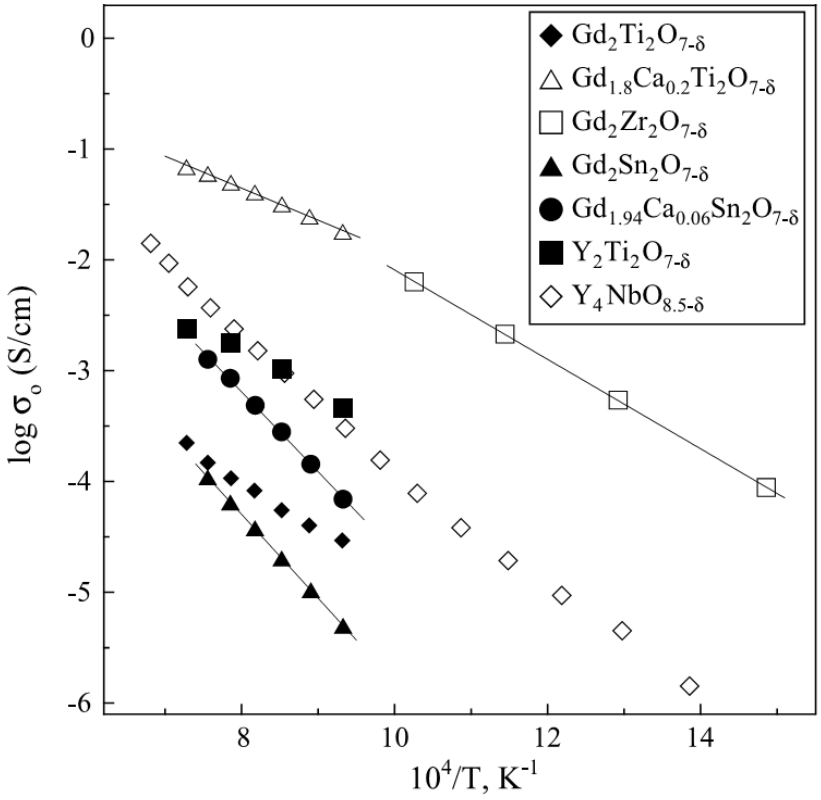

Fig. 10. Oxygen ionic conductivity of selected pyrochlores in air [15].

Acceptor-type doping by calcium leads to formation of oxygen vacancies to maintain the electroneutrality of the lattice. The reaction of substitution and formation of vacancies can be described as (using Kroger-Vink notation):

$$2CaO + 2TiO_2 \xrightarrow{Gd_2Ti_2O_7} 2Ca'_{Gd} + 2Ti^{x}_{Ti} + 6O^{x}_{O} + V^{\bullet\bullet}_{O} \qquad (3)$$

Electroneutrality conditions: $[V^{\bullet\bullet}_{O}] = 0.5[Ca'_{Gd}]$

Oxygen vacancies make it possible for oxygen ions to move from its positions to neighbouring vacant sites and thus to diffuse through oxygen subblattice under gradient of concentration or electrical potential. Hopping of oxygen ions between two neighbouring atomic

positions requires to overcome the potential energy barrier, and therefore ionic conductivity increases with increasing of temperature.

In accordance with equation (3), the increase in the concentration of the dopant (Ca^{2+}) should increase the concentration of oxygen vacancies and, consequently, specific ionic conductivity. At low level of doping, the dependence of the ionic conductivity on the concentration can be expected to be be linear.

In general case, substitution may be continuous with formation of entire concnetrational range of solid solutions, may or reach a limit, depending on the nature of host lattice, similarity of ionic radii of dopant, and equivalence of oxidation state. In the case of gadolinium substitution by calcium, an increase in the concentration of Ca'_{Gd} eventually leads to a precipitation of secondary phase - $CaTiO_3$. In terms of highest ionic conductivity and phase stability, the optimal level of substitution of gadolinium by calcium in $(Gd_{1-x}Ca_x)_2Ti_2O_7$ corresponds to the range x = 0.05–0.10 (Fig. 11).

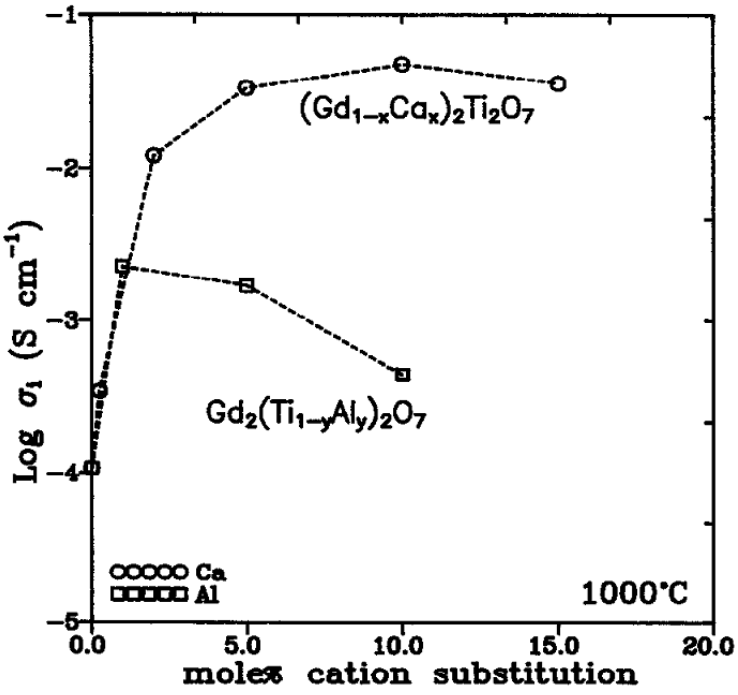

Fig. 11. Ionic conductivity of $(Gd,Ca)_2Ti_2O_7$ at 1000°C as a function of acceptor dopant concentration [1].

Further increase of calcium concentration (above 10mol%) in A^{3+}-sublattice does not results in increase of conductivity. This can be explained by two factors: precipitation of second phase and association of defects, which reduced the mobility of ionic charge carriers:

$$V_O^{\bullet\bullet} + Ca'_{Gd} \Rightarrow (V_O Ca_{Gd})^{\bullet} \qquad (4)$$

In contrast to Ca doping, molybdenum substitution results in a formation of entire continuous series of $Gd_2(Ti,Mo)_2O_7$ solid solution with pyrochlore-type structure, under reducing conditions. This is possible due to the fact that molybdenum has ionic radii very close to the radius of Ti^{4+} and may exist in several oxidation states: 4+, 5+, 6+. Since the most stable oxidation state of molybdenum cation under oxidizing conditions is 6+, pyrochlore-type solid solutions with high Mo-content are stable only under reducing conditions, where oxidation states of molybdenum can be 5+ and 4+. Taking into account practical requirements for phase stability of anode material in a wide oxygen partial pressure range, doping by molybdenum should be moderate. Therefore, one of the aims of present work is to find a compromise between phase stability and suitable transport properties since they have inverse dependence.

Substitution of titanium by molybdenum in $Gd_2Ti_2O_7$ induces high electronic conductivity. Total electrical conductivity increases with molybdenum content: up to 70 S/cm at 1000°C for composition $Gd_2(Ti_{0.3}Mo_{0.7})_2O_7$ [3] and up to ~150 S/cm for $Gd_2Mo_2O_7$ at room temperature [16]. Targeting the phase stability in wide range of pO_2, the level of Mo-doping for studies of electrical and electrochemical properties in this work was chosen in a range y=0-0.2 for $(Gd,Ca)_2(Ti_{1-y}Mo_y)_2O_7$.

1.5. Objectives of this works

The main objective of the work is the design and comprehensive characterization of solid solutions derived from the pyrochlore-type $Gd_2Ti_2O_7$ by co-substitutions of Gd and Ti by Ca and Mo, respectively, for prospective electrocatalytic applications.

Particular objective include:

- to evaluate phase relationships in $(Ga,Ca)_2(Ti,Mo)_2O_{7\pm\delta}$ system;
- to assess redox changes on cycling between oxidizing and reducing conditions;
- to study of ionic and electronic transport properties under variaety of $p(O_2)$-T-humidity conditions;
- to model defect chemistry of solid solutions based on experimental results;
- to evaluate thermomechanical stability and thermochemical compatibility with other cell materials.

Chapter 2. Experimental

2.1. Materials preparation

Synthesis of $(Gd_{1-x}Ca_x)_2Ti_2O_7$ (x=0.025, 0.05, 0.07) and $(Gd_{1-x}Ca_x)_2(Ti_{1-y},Mo_y)_2O_7$ (x=0.07, 0.10; y=0.05, 0.10) solid solutions was performed by conventional solid-state reaction route with repeated calcinations and grindings in agate mortar. Solid-state synthesis was chosen because of simplicity. Flow chart of synthesis and ceramic processing route is presented in Fig. 12. Gadolinium and titanium oxides were preliminary annealed in order to remove adsorbed moisture before weighing. Initial reagents decompose and react during several annealings with formation of pyrochlore phase. Intermediate grindings helps to achieve uniform distribution of cations. Sintering temperature of $(Gd,Ca)_2(Ti,Mo)_2O_7$ ceramics was in the range 1600-1700°C. Such a high temperature is necessary to obtain dense and gas-tight samples. Final sintering was performed with using Pt foil as support and powder cover with the same cation composition for prevention of possible high temperature losses. Heating/cooling rate was in a range 3-5°C per minute.

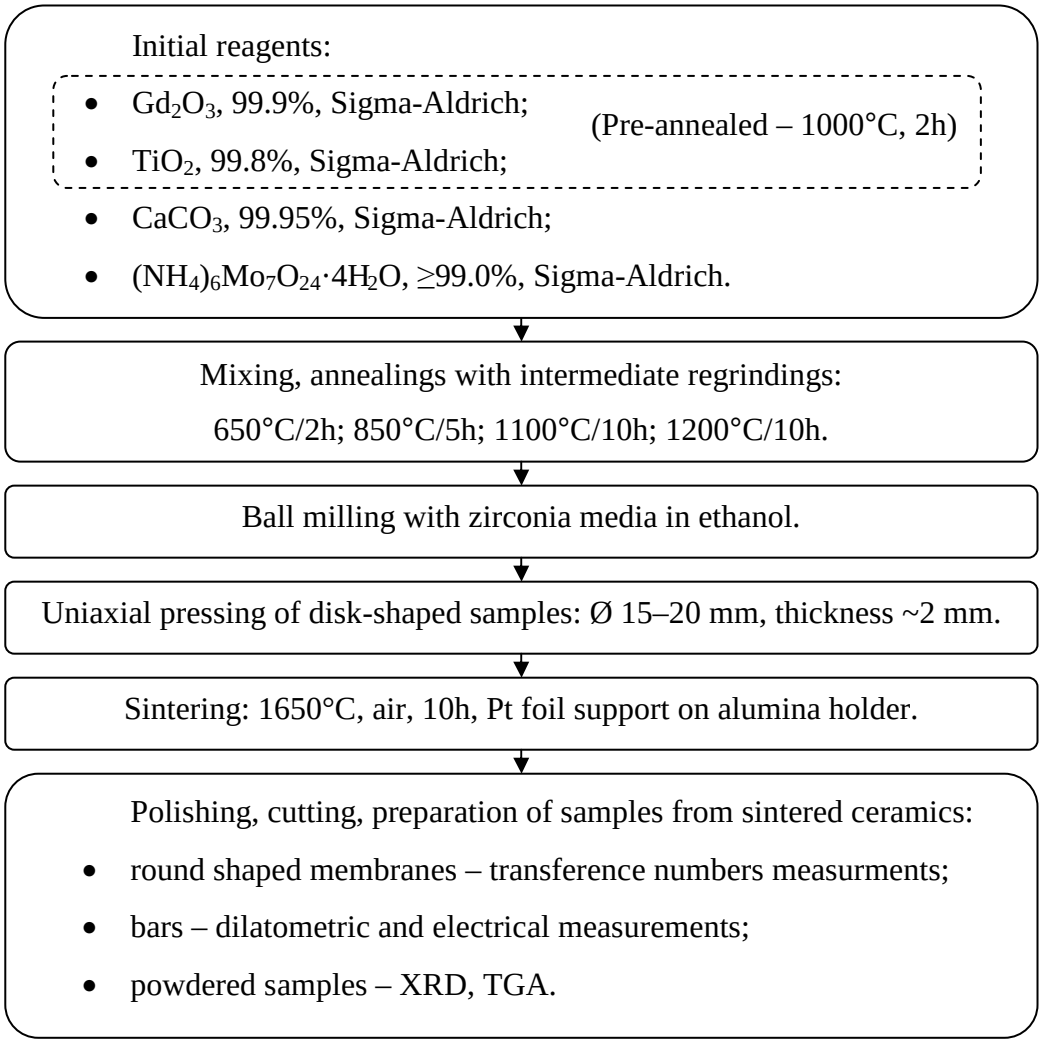

Fig. 12. Flow chart of ceramic synthesis and processing.

Density of sintered dense samples was calculated from the mass and volume of round pellets with uniform thickness. Gas-tightness test involved gluing a membrane to a tube and applying pressure in ~2 atm of air from one side. Bar-shaped samples were cut with using Struers cut-off machine and diamond wheel.

2.2 Characterization techniques

X-ray powder diffraction

The phase composition of sintered ceramics and reduced samples was analyzed by X-ray powder diffraction. Spectra were recorded with using PANalytical X'Pert PRO diffractometer (CuKα radiation) with angular resolution 0.02° in the range 2Θ = 20-80°. Lattice parameters and theoretical density were calculated by Rietveld refinement of the diffraction spectra in FullProf software. Atomic coordinates for pure $Gd_2Ti_2O_7$ were taken as initial parameters for Rietveld refinement (Table 2). Comparison of densities, theoretically calculated and geometrically measured, allows to calculated relative density of sintered ceramics.

Microstructural analysis

Scanning electron microscopy (SEM) is a standard technique to monitor microstructure of ceramics. It allows measuring sizes and morphology of grains. Surface of samples can be prepared for SEM in several ways - it can be fractured (by breaking the sample mechanically) or polished. In present work, SEM analysis were performed only for fractured samples for control of minor phase impurities and porosity using Hitachi SU-70 microscope. Thin carbon layer was deposited in a vacuum on the surface of samples for discharge of sample surface under electron beam.

AC impedance spectroscopy

Impedance spectroscopy allows studying mechanism of electrical transport in materials and electrochemical cells. Application of external potential difference to symmetrical solid electrolyte cell do not lead to instant stabilization of electrical current and have relaxation time due to presence of electrical reactance (inductance or capacitance) of crystal lattice, dipoles, ionic chemical bonds, recharging of grain/interphase boundaries. Under AC current some part of energy is spent on recharging of reactance elements with properties of capacitor or inductor. It causes to a phase shift between current and voltage. Phase shift allows determining contribution of reactance, which represents an imaginary part in total resistivity – Z'' on Fig. 13. Processes have different kinetics and relaxation times. It is resulting in a non-linear response of the

electrochemical system to applied alternating current with variation of frequency. Polarization processes can be divided into three main groups by relaxation time:

- fast processes – relaxation of ionic chemical bonds and positions of ions in crystal lattice (shifting of ions and valence electrons under potential difference);
- medium – recharging of grain boundaries;
- slow – surface exchange processes on electrodes.

Each of these three main groups of processes introduces an impact on imaginary part of impedance spectra for different region of frequency. Typical impedance spectra of symmetrical solid electrolyte cell are represented on Fig. 13. Impedance spectroscopy allows to separate contributions of each element of electrochemical system (grains, grain boundaries, and electrodes) in total resistivity since the relaxation time of each element differs by several orders of magnitude. Equivalent electrical circuit allows interpretation and fitting of spectra to find capacitance and resistance of each element.

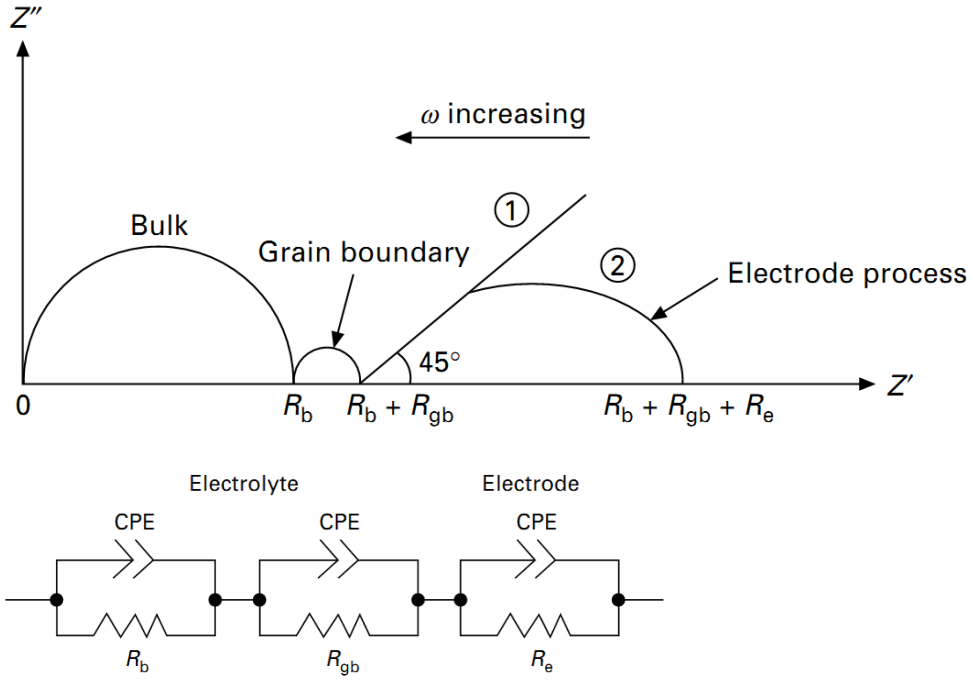

Fig. 13. Typical impedance spectrum of solid electrolyte symmetrical cell and equivalent electrical circuit (ω -current frequency, CPE – constant-phase-element) [4, p.158].

By value of capacitance of semicircle it is possible to match it with element of electrochemical system. Typical values of capacitance and related processes are presented in Table 3. Due to overlapping of relaxation times of phenomena and capacitances of elements, semicircles may overlap each other and shape of impedance spectra became more complicated. Most complicated part is electrode processes, since kinetics of electrode processes depends on

microstructure of electrodes, quality of membrane-electrode interface and composition of the gas phase. Additional difficulty is that comprehensive studying of electrode processes requires low AC frequencies – below 20Hz.

Table 3. Capacitance values and their possible interpretation [17, 18]

Capacitance, F/cm	Phenomenon responsible
10^{-12}	bulk
10^{-11}	minor/second phase
$10^{-11} – 10^{-8}$	grain boundary
$10^{-10} – 10^{-9}$	bulk ferroelectric near T_C (Curie Temperature)
$10^{-9} – 10^{-7}$	surface layer
$10^{-7} – 10^{-5}$	sample-electrode interface
10^{-4}	electrochemical reactions

In present work, AC impedance spectroscopy was used for measurements of total electrical conductivity of the materials as function of temperature and oxygen partial pressure. Additional experiments in dry and wet gases were performed for assessment of contribution of proton conduction to the total conductivity. Platinum was used as electrode material and as current collectors during high-temperature measurements. The measurements were performed in controlled atmospheres: air, inert gas (Ar), O_2, 10%H_2-N_2, and their mixtures to vary oxygen partial pressure. Specific conductivity was calculated using the expression:

$$\sigma = \frac{L}{R \cdot S} \tag{5}$$

R – resistance of sample (R_{bulk} or $R_{bulk}+R_{grain\ boundary}$)

S – cross-sectional area of sample

L – length of sample

Dry and humidified gases were used to control humidity of atmosphere. Equipment allows varying frequency of current in a range 20 – 10^6 Hz (Agilent 4284A precision LCR meter).

Transport numbers measurements

To separate the contributions of oxygen-ions and electrons to the total conductivity, transference numbers were determined employing modified e.m.f. technique, which is described in details in [19, 20, 21]. This technique allows measuring the transference numbers of mixed ionic-electronic conductors with relatively small electronic contribution. Scheme of experimental

setup represented on Fig. 14. Sample is a disk-shaped membrane with thickness ~1 mm and internal diameter ~9 mm. Platinum electrodes and contacts were applied to the sample before measurements by painting with platinum paste and annealing at 900°C. Measurements were performed under oxygen partial pressure difference across membrane: external side - air; internal volume - pure oxygen, argon or 10%H_2-N_2 mixture. Transference numbers were determined at 700–950°C. Modified e.m.f. technique makes it possible to take into account the effect of electrode polarization on experimentally measured values of e.m.f. by analyzing its dependence on external load [19, 20, 21]. External loads R_M used for measurements were in a range hundreds Ohms – 100 kOhm.

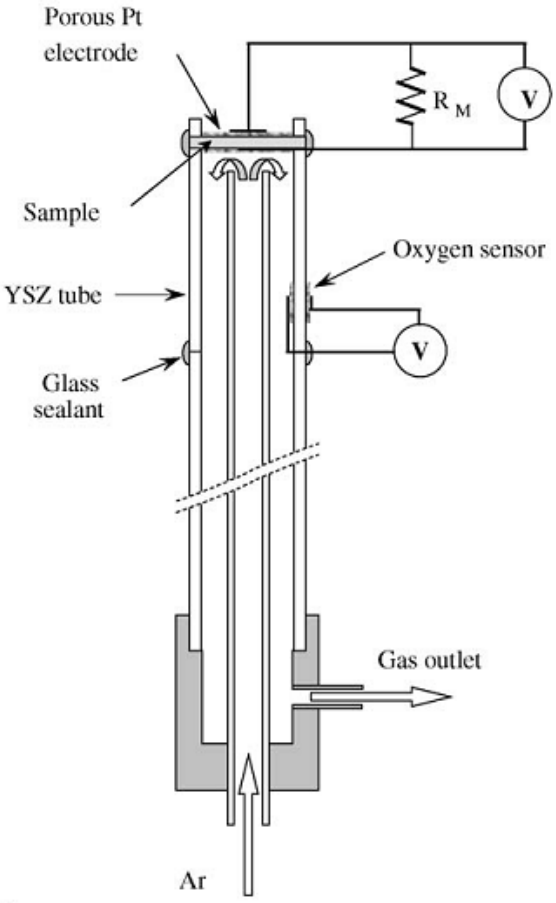

Fig. 14 Schematic drawings of the experimental setups for the modified e.m.f. technique [20].

Dilatometry

Thermal and chemical expansion leads to a change in the dimensions of SOFC components. It is important to know thermal expansion coefficients (TEC) of new materials for assessment of its thermomechanical compatibility with other SOFC materials. Dimensional changes of ceramic materials with variations of temperature and oxygen partial pressure were determined by controlled-atmosphere dilatometry using vertical Linseis L75V/1250 instrument.

Measurements were performed in atmosphere of air, argon and CO-CO_2 mixtures in temperature range between room temperature and 1100°C.

Thermogravimetric analysis

Thermogravimetry (TGA) allows to measure small variations in weight of sample caused by chemical decomposition, phase transitions and exchange processes with atmosphere. Variations in temperature and partial oxygen pressure may lead to changes in oxygen nonstoichiometry of the sample. In reducing conditions oxygen may escape from the crystal lattice in gas phase according with equilibrium $O_O^{\times} \xleftrightarrow{k_{red}} V_O^{\bullet\bullet} + 2e' + 0.5O_2$, thus affecting the weight of sample; variation in weight allows to calculate oxygen nonstoichiometry or its change. TGA data may clarify mechanisms of defect formation by comparison data of weight changes with impedance spectroscopy in the same conditions. In present work, TGA was performed using Setaram SetSys 16/18 instrument. Measurements were done in a temperature range between room temperature and 1000°C under atmosphere of air, argon or mixture of 10% H_2 in N_2.

Chapter 3. Results

3.1. Phase relationships and structural characterization

XRD patterns of as-prepared ceramic materials are given in Fig. 15. $(Gd_{1-x}Ca_x)_2Ti_2O_7$ (x = 0.025-0.07) and $(Gd_{1-x}Ca_x)_2(Ti_{0.95}Mo_{0.05})_2O_7$ (x =0.07–0.10) were found to be phase-pure with cubic pyrochlore-type structure (space group Fd-3m) isostructural to the parent $Gd_2Ti_2O_7$. Increasing molybdenum concentration in x = 0.07–0.10 compositions to 10% of titanium sites results in a minor precipitation of tetragonal $CaMoO_4$ phase, possibly because the prevailing oxidation state of molybdenum cations under oxidizing conditions is 6+, and the pyrochlore structure has limited ability to tolerate oxygen hyperstoichiometry. On the other hand, increasing calcium content in $(Gd_{1-x}Ca_x)_2(Ti_{0.95}Mo_{0.05})_2O_7$ above x = 0.10 was found to promote the segregation of orthorhombic $CaTiO_3$ phase impurity, which is a stable perovskite phase. Thus, one may conclude that the $(Gd_{1-x}Ca_x)_2(Ti_{1-y},Mo_y)_2O_{7-\delta}$ solid solution field at ambient $p(O_2)$ is limited to $0.10 < x < 0.15$ and $0.05 < y < 0.10$.

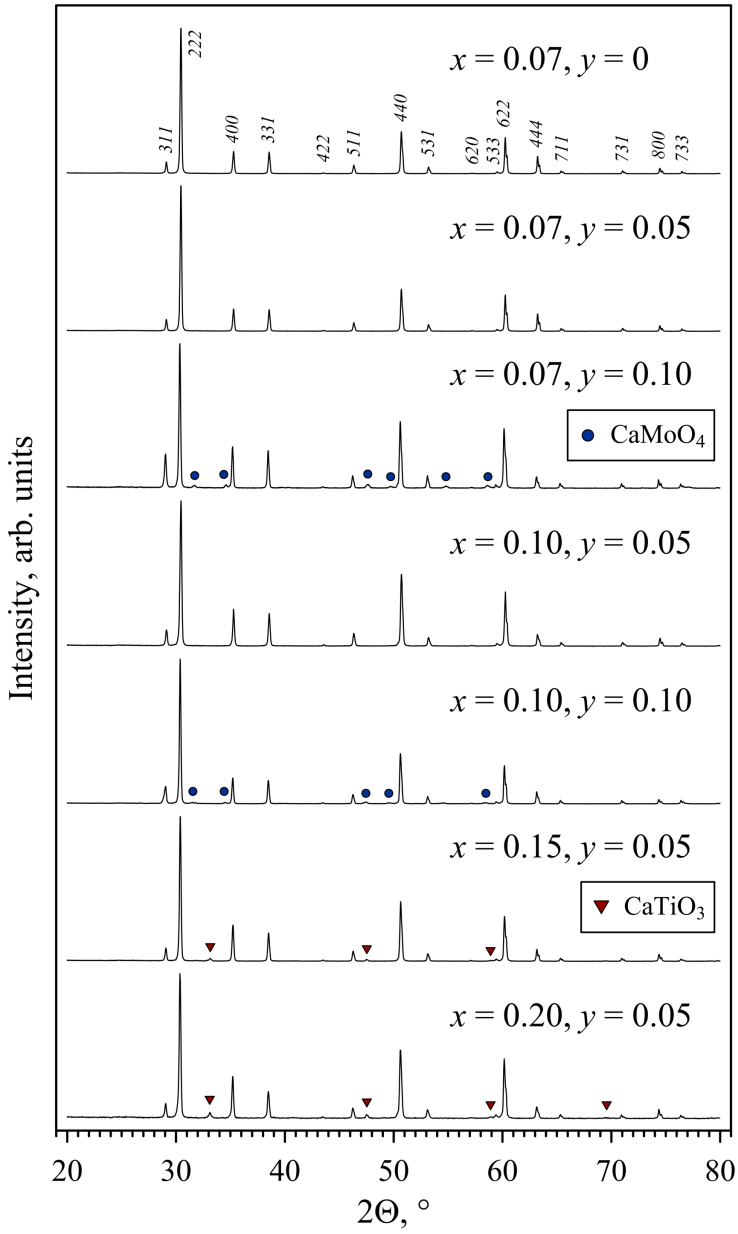

Fig. 15. XRD patterns of as-prepared $(Gd_{1-x}Ca_x)_2(Ti_{1-y},Mo_y)_2O_{7-\delta}$ ceramics. *hkl* indexes are given for Fd-3m space group. Reflections of $CaMoO_4$ and $CaTiO_3$ impurities are indexed according to JCPDS PDFs: $CaMoO_4$ – # 85-1267, $CaTiO_3$ – # 88-0790.

Substitutions have rather minor influence on the lattice parameters of single-phase solid solutions (Table 4). Lattice constants increase slightly with calcium content due to the moderate differences between ionic radii of calcium and gadolinium cations ($r^{VIII}_{Gd^{3+}} = 1.053$ Å vs. $r^{VIII}_{Ca^{2+}} = 1.12$ Å) [14]. Note that one neglects anti-site exchange due to major differences in ionic radii of A-site cations (Ca^{2+} and Gd^{3+}) and B-site cations in their expected valence states (Ti^{4+} and Mo^{6+}). Molybdenum has tendency to higher 6+ oxidation state under oxidizing conditions, with an ionic radius very similar to that of Ti^{4+} ($r^{VI}_{Ti^{4+}} = 0.605$ Å, $r^{VI}_{Mo^{6+}} = 0.59$ Å) [14]. However, this depends on the redox conditions, and possibly also on the Mo:Ca ratio. In fact, the average valence of

molybdenum cations in some pyrochlores is close to Mo^{5+}, namely, in oxynitride pyrochlores. Thus, one may expect a fraction of lower valence cations (Mo^{4+} or Mo^{5+}), mainly when $y > 0.5x$. All prepared ceramics were dense and gas-tight; the relative densities of single-phase materials were 93–96% of theoretical (Table 4)

Table 4. Unit cell parameters and densities of single-phase $(Gd_{1-x}Ca_x)_2(Ti_{1-y},Mo_y)_2O_7$ compositions. Reducing conditions: 36h, 950°C, pO_2 ~10^{-19} atm.

Composition	State	Lattice parameters		Density, g/cm^3	Relative density, %
		a, Å	*X (O^{2-}, 48f)*		
x = 0.07, y = 0	Oxidized	10.1929(4)	0.3189(6)	6.07	96
x = 0.07, y = 0.05	Oxidized	10.1931(2)	0.3140(7)	5.94	93
	Reduced	10.1933(5)	0.3166(9)	-	-
x = 0.10, y = 0.05	Oxidized	10.1937(5)	0.3277(7)	6.02	95
	Reduced	10.1941(5)	0.3150(8)	-	-

3.2. Microstructural characterization

SEM studies confirmed high density of sintered samples. Examples of SEM micrographs of fractured ceramics are given in Fig. 16. Other samples have similar dense microstructures with low porosity and with grains size in a range 5-20 μm. Microstructure is typical for such types of ceramics sintered at high temperatures.

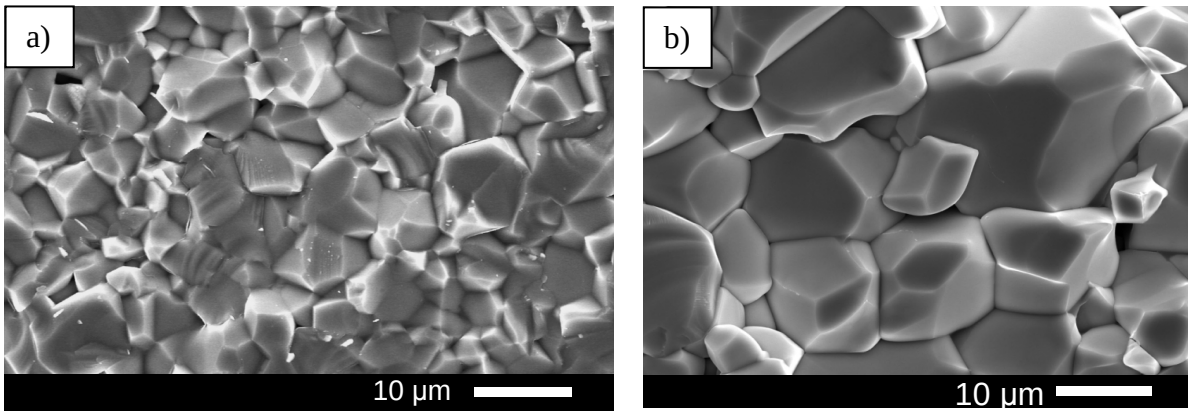

Fig. 16. SEM micrographs of fractured $(Gd_{0.975}Ca_{0.025})_2Ti_2O_7$ (a) and $(Gd_{0.93}Ca_{0.07})_2(Ti_{0.95}Mo_{0.05})_2O_7$ (b) after sintering in air.

3.3. Reducibility and phase stability under reducing conditions

Thermogravimetric analysis demonstrated that powdered $(Gd_{1-x}Ca_x)_2(Ti_{1-y}Mo_y)_2O_{7-\delta}$ samples start to lose oxygen from the crystal lattice on heating above ~300°C in reducing 10% H_2–N_2 atmosphere (Fig. 17). The reduction in the studied temperature range was found to occur in two steps. The lower-temperature process had maximum rate at ~640°C under applied experimental conditions, while the second process starts to accelerate at T > 870°C.

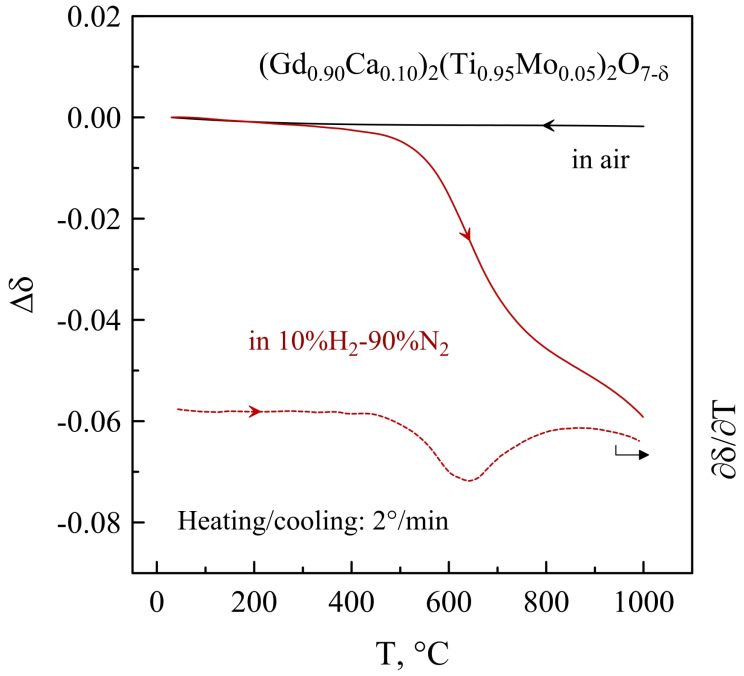

Fig. 17. Relative changes of oxygen nonstoichiometry in $(Gd_{0.9}Ca_{0.1})_2(Ti_{0.95}Mo_{0.05})_2O_{7-\delta}$ on cooling in air and on heating in reducing atmosphere, and derivative thermogravimetric curve on heating in reducing atmosphere.

Isothermal studies at 950°C confirmed that reduction is a two-step process (Fig. 18). While the oxygen content in the samples remains unchanged (within experimental uncertainty) in air and in inert atmosphere, switching to reducing atmosphere results in nearly instant release of oxygen. This is followed by further slow oxygen losses from the samples.

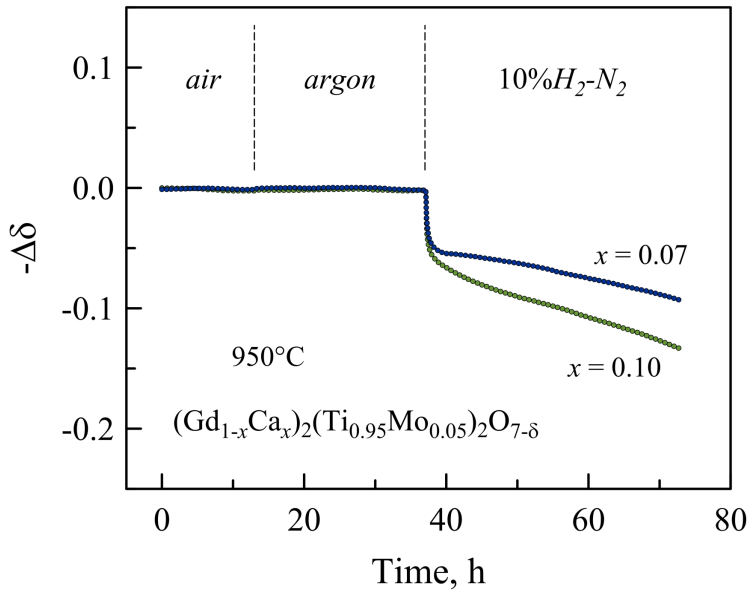

Fig. 18. Relative changes of oxygen nonstoichiometry in $(Gd_{1-x}Ca_x)_2(Ti_{0.95}Mo_{0.05})_2O_{7-\delta}$ on isothermal reduction at 950°C, as estimated from the thermogravimetric data.

Oxygen losses Δδ from the lattice of $(Gd_{1-x}Ca_x)_2(Ti_{0.95}Mo_{0.05})_2O_{7-\delta}$ in the first fast step were roughly estimated to be ~0.051 oxygen atoms per formula unit for x = 0.07 and 0.060-0.067 atoms per formula unit for x = 0.10. Note that a decrease of oxidation state of molybdenum by 1 in the given compositions corresponds to change of oxygen content of 0.05 oxygen atoms per formula unit. Thus, one may assume that the first reduction step corresponds to comparatively fast $Mo^{6+} \rightarrow Mo^{5+}$ change, whereas the second comparatively slow step can be assigned to slower $Mo^{5+} \rightarrow Mo^{4+}$ transformation; this may raise doubts about previous indications that the intermediate oxidation state Mo^{5+} is highly unstable [22]. One may even assume also onset of partial $Ti^{4+} \rightarrow Ti^{3+}$ or even $Mo^{4+} \rightarrow Mo^{3+}$ reduction, on exceeding the oxygen storage ability of previous $Mo^{6+} \rightarrow Mo^{5+} \rightarrow Mo^{4+}$ changes. Although 3+ is a rather unusual state for molybdenum in oxide compounds, the presence of Mo^{3+} in reduced molybdenum oxide has been previously suggested in the literature based on the XPS results [23]. The oxygen nonstoichiometry range of $MoO_{2\pm\delta}$ [24, 25] also indicates the presence of a fraction of Mo cations in an oxidation state lower than 4+.

Table 5. Oxygen nonstoichiometry of $(Gd_{1-x}Ca_x)_2(Ti_{1-y},Mo_y)_2O_{7-\delta}$ compositions. Reducing conditions: 36h, 950°C, pO_2 ~10^{-19} atm.

Composition	State	Oxygen nonstoichiometry, 7-δ[a]
x = 0.07, y = 0	Oxidized	6.93
x = 0.07, y = 0.05	Oxidized	7.03
	Reduced[b]	6.94
x = 0.10, y = 0.05	Oxidized	7.00
	Reduced[b]	6.87

[a] Estimated assuming all Mo cations in oxidized phases to be in 6+ oxidation state.

[b] After 36h, 950°C, pO_2 ~10^{-19} atm.

XRD analysis of powdered $(Gd_{1-x}Ca_x)_2(Ti_{0.95}Mo_{0.05})_2O_{7-\delta}$ samples after reduction in 10% H_2–N_2 flow ($p(O_2)$ ~10^{-19} atm) at 950°C for 36 h did not reveal any significant changes in XRD patterns (Fig. 19), except the appearance of tiny unidentified peaks on the background level. The minor increase of lattice parameters is also comparable to experimental error (Table 4). Table 5 lists also the values of oxygen nonstoichiometry of reduced pyrochlores estimated assuming that all Mo cations in oxidized phases were hexavalent. One should also note that even after 36 h of reduction the oxygen content does not tend to a constant value, indicating very slow reduction kinetics. Though this is less sluggish than reported for perovskite-like donor-doped strontium titanates at temperatures ≤1000°C, the long-term stability under applied conditions remains uncertain; the $p(O_2)$ value in the course of reduction was below the Mo/MoO_2 boundary and also below the stability boundary of $Gd_2(Ti_{0.3}Mo_{0.7})_2O_{7-\delta}$. [3].

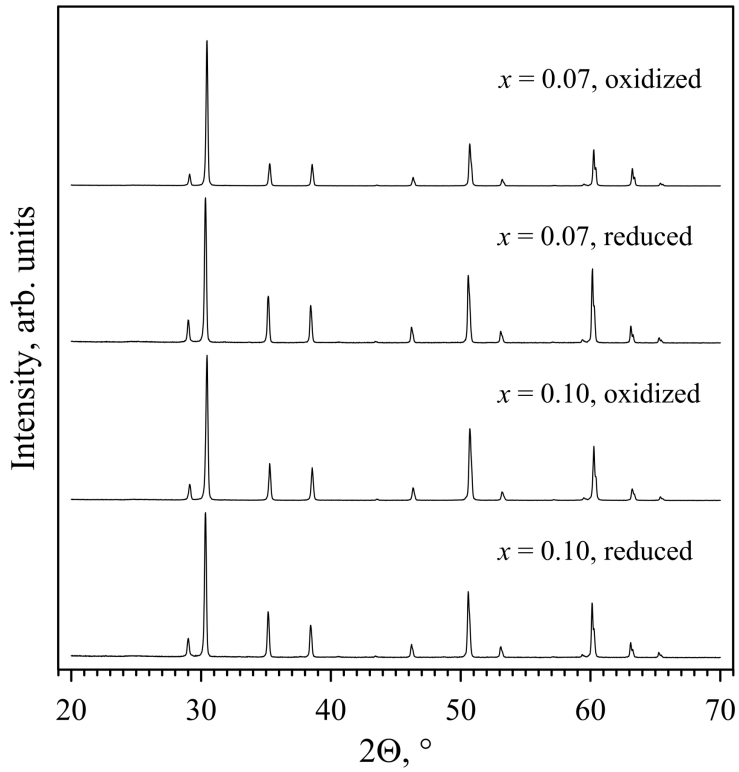

Fig. 19. XRD patterns of $(Gd_{1-x}Ca_x)_2(Ti_{0.95}Mo_{0.05})_2O_{7-\delta}$ compositions sintered in air (oxidized) and reduced in powdered form under hydrogen atmosphere (36h, 950°C, pO_2 ~10^{-19} atm).

3.4. Electrical conductivity in air

3.4.1. Total conductivity

AC impedance spectroscopy was used to determine total conductivities of two series of compositions (Ca-doped and Ca&Mo co-doped) as function of temperature. Total resistivities of samples were determined as a sum of bulk and grain boundary resistances by fitting of impedance spectra. The correlation of total conductivity with the level of calcium doping in the compositions $(Gd_{1-x}Ca_x)_2Ti_2O_{7-\delta}$ (x = 0.025, 0.05, 0.07) (Fig. 20) is in full accordance with the literature data [1]. Acceptor doping leads to vacancy formation for charge compensation. An increase in the concentration of vacancies leads to an increase in oxygen ionic conductivity and, consequently, total conductivity. Concentration of dopant – *x* is equal to level of oxygen nonstoichiometry – δ in formula unit.

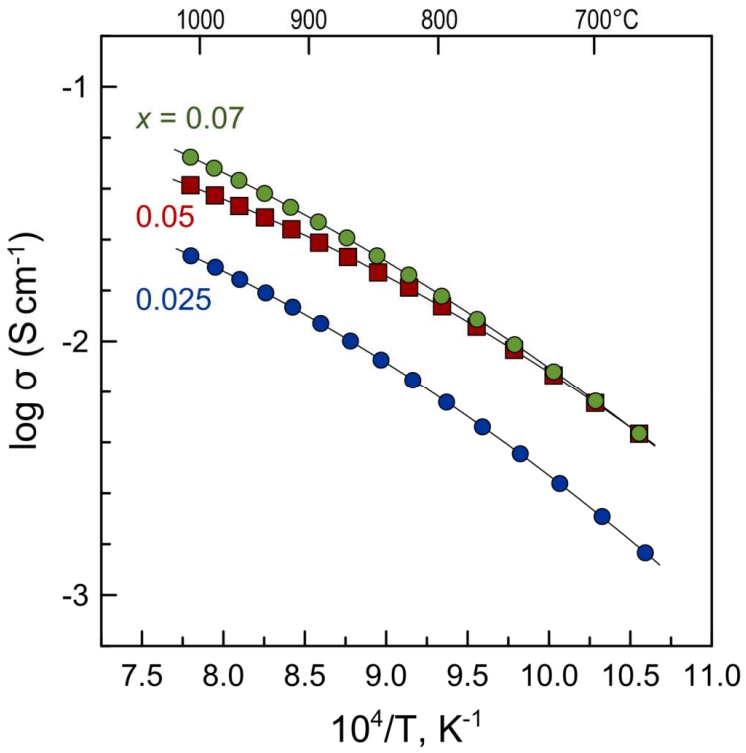

Fig. 20. Temperature dependence of total conductivity of $(Gd_{1-x}Ca_x)_2Ti_2O_{7-\delta}$ ceramics in dry air.

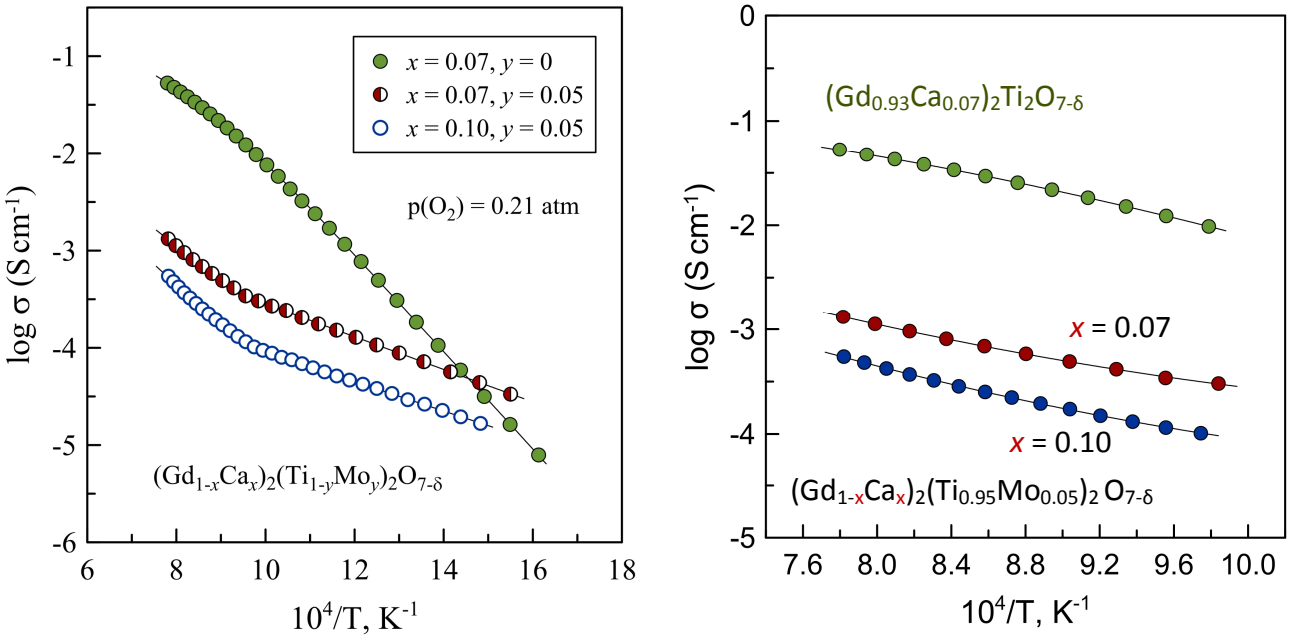

Fig. 21. Temperature dependence of total conductivity of $(Gd_{1-x}Ca_x)_2(Ti_{1-y}Mo_y)_2O_{7-\delta}$ ceramics in dry air. Right plot: enlarged high-temperature region.

Substitution of 5% of titanium by molybdenum results in suppression of ionic transport in $(Gd_{1-x}Ca_x)_2(Ti_{0.95}Mo_{0.05})_2O_{7-\delta}$ and a significant drop in electrical conductivity (Fig. 21). This phenomenon can be explained by taking into account charge compensation for acceptor and

donor co-substitution. Acceptor-type substitution by calcium is expected to be compensated by formation of oxygen vacancies, while donor-type substitution by $Mo^{5+/6+}$ may be compensated by incorporation of interstitial oxygen ions (*e.g.* into *8a* sites):

$$Gd_2O_3 + 2MoO_3 \xrightarrow{Gd_2Ti_2O_7} 2Gd_{Gd}^{\times} + 2Mo_{Ti}^{\bullet\bullet} + 2O_i'' + 7O_o^{\times} \quad (6)$$

and co-additions of acceptor and donor may compensate each other. Thus, a general electroneutrality condition for $(Gd_{1-x}Ca_x)_2(Ti_{1-y},Mo_y)_2O_{7-\delta}$ is, therefore, expressed by:

$$[Ca_{Gd}'] + 2[O_i''] + n = 2[Mo_{Ti}^{\bullet\bullet}] + [Mo_{Ti}^{\bullet}] + 2[V_O^{\bullet\bullet}] + p \quad (7)$$

where $[Ca_{Gd}'] = 2x$,

$[Mo_{Ti}^{x}] + [Mo_{Ti}^{\bullet\bullet}] + [Mo_{Ti}^{\bullet}] = 2y$,

$[V_O^{\bullet\bullet}] - [O_i''] = \delta$,

and $[Mo_{Ti}^{x}] \equiv Mo^{4+}$, $[Mo_{Ti}^{\bullet}] \equiv Mo^{5+}$ and $[Mo_{Ti}^{\bullet\bullet}] \equiv Mo^{6+}$ respectively, per formula unit. Variations of electrical conductivity and partial ionic contribution with composition reflect a transition between dominating compensation mechanisms under oxidizing conditions: from acceptor compensation via oxygen vacancy formation in $(Gd_{1-x}Ca_x)_2Ti_2O_{7-\delta}$:

$$[V_O^{\bullet\bullet}] = 0.5[Ca_{Gd}'] \text{ or } \delta = x \quad (8)$$

to donor compensation via interstitial oxygen formation in hyperstoichiometric $(Gd_{0.93}Ca_{0.07})_2(Ti_{0.95}Mo_{0.05})_2O_{7-\delta}$ (assuming predominant 6+ state of Mo cations):

$$[O_i''] = [Mo_{Ti}^{\bullet\bullet}] - 0.5[Ca_{Gd}'] \text{ or } -\delta = 2y-x \quad (9)$$

Apparently, incorporation of extrinsic interstitial oxygen strongly suppresses the concentration of oxygen vacancies originating from intrinsic anti-Frenkel disorder:

$$O_O^{x} \leftrightarrow V_O^{\bullet\bullet} + O_i''; \qquad k_{aF} = [V_O^{\bullet\bullet}][O_i''] \quad (10)$$

if one assumes prevailing hexavalent Mo^{6+} and that the difference between donor and acceptor contributions play a prevailing effect which exceeds largely the contribution of anti-Frenkel disorder, $[Mo_{Ti}^{\bullet\bullet}] - 0.5[Ca_{Gd}'] \approx 2y - x >> k_{aF}^{1/2}$ and thus:

$$[V_O^{\bullet\bullet}] = \frac{k_{aF}}{[O_i'']} \approx \frac{k_{aF}}{2y - x} \quad (11)$$

This explains a decrease in oxygen-ionic conductivity occurring via oxygen vacancy migration between 48f sites. Note that decline in ionic conductivity with niobium substitution

was reported earlier for the $Yb_2(Ti_{1-y}Nb_y)_2O_7$ system, although the authors claimed that Nb substituted in a 4+ oxidation state and attributed the decrease of ionic transport to trapping of oxygen anions by dopant cations [26].

Finally, in $(Gd_{0.90}Ca_{0.10})_2(Ti_{0.95}Mo_{0.05})_2O_{7-\delta}$, acceptor and donor nearly compensate each other:

$$[Ca'_{Gd}] = 2[Mo^{\bullet\bullet}_{Ti}] \quad (12)$$

while oxygen vacancy concentration is governed, most likely, by the intrinsic contribution of anti-Frenkel disorder (eqn. (10)). These changes of compensation mechanism results in a transition from predominantly ionic (for exclusive acceptor additive, x = 0.07 and y = 0) to predominantly electronic (for $2y > x$) and then to mixed ionic-electronic transport (for $2y = x$) under oxidizing conditions, as shown in section 3.4.3.

The activation energy of total conductivity was calculated using Arrhenius model:

$$\sigma = \frac{A_0}{T}\exp\left(\frac{E_a}{RT}\right) \quad (13)$$

Decreasing temperature below ~780°C results in an increase in activation energy of $(Gd_{0.93}Ca_{0.07})_2Ti_2O_{7-\delta}$ (Fig. 21 and Table 6). Change in a slope of Arrhenius dependencies of electrical conductivity is characteristic of many oxygen-ion conductors, including fluuorite-type stabilized zirconia and doped ceria [27], pyrochlore-type $Gd_2(Ti_{1-y}Zr_y)_2O_7$ [28], and perovskite-type $(La,A)(Ga,Mg)O_{3-\delta}$ [29], and is usually ascribed to partial ordering in the oxygen sublattice due to point defect association in the low-temperature range.

Contrary to $(Gd_{0.93}Ca_{0.07})_2Ti_2O_{7-\delta}$, Arrhenius dependencies of total electrical conductivity of Mo-substituted ceramics show a transition from high-T regime with higher activation energy (74–85 kJ mol^{-1}) to low-T regime with lower E_A (37–39 kJ mol^{-1}) (Fig. 21 and Table 6). Similar behavior was reported for $Gd_2(Ti_{1-y}Nb_y)_2O_7$ (y = 0.01–0.10) pyrochlores, although under quenched conditions and at lower temperatures, with lower activation energy attributed to electron hopping between Nb^{4+} and Nb^{5+} [30].

Table 6. Activation energy of total conductivity $(Gd_{1-x}Ca_x)_2(Ti_{1-y}Mo_y)_2O_{7-\delta}$ in air.

Composition	T°C	E_a, kJ/mol
x = 0.07, y = 0	250–780	99.8 ± 0.5
	780–1010	77.1 ± 1.0
x = 0.07, y = 0.05	370–770	39.2 ± 0.2
	770–1010	73.6 ± 1.3
x = 0.10, y = 0.05	400–780	36.6 ± 0.3
	780–1010	85.2 ± 1.6

Another comment is that the electrical conductivity data for $(Gd_{1-x}Ca_x)_2(Ti_{1-y}Mo_y)_2O_{7-\delta}$ ceramics doped beyond the solid solubility limits (Fig. 22) seem to support the above conclusion that solid solution formation field extends to x ~ 0.125 and y ~ 0.075. This is reflected by increased conductivity for x = 0.15 (higher ionic transport induced by acceptor substitution) and for y = 0.10 (probably, due to increased electronic transport contributed by electronic hopping between Mo^{6+} and residual Mo^{5+}) as compared to single phase $(Gd_{1-x}Ca_x)_2(Ti_{1-y}Mo_y)_2O_{7-\delta}$ (x = 0.07–0.10)

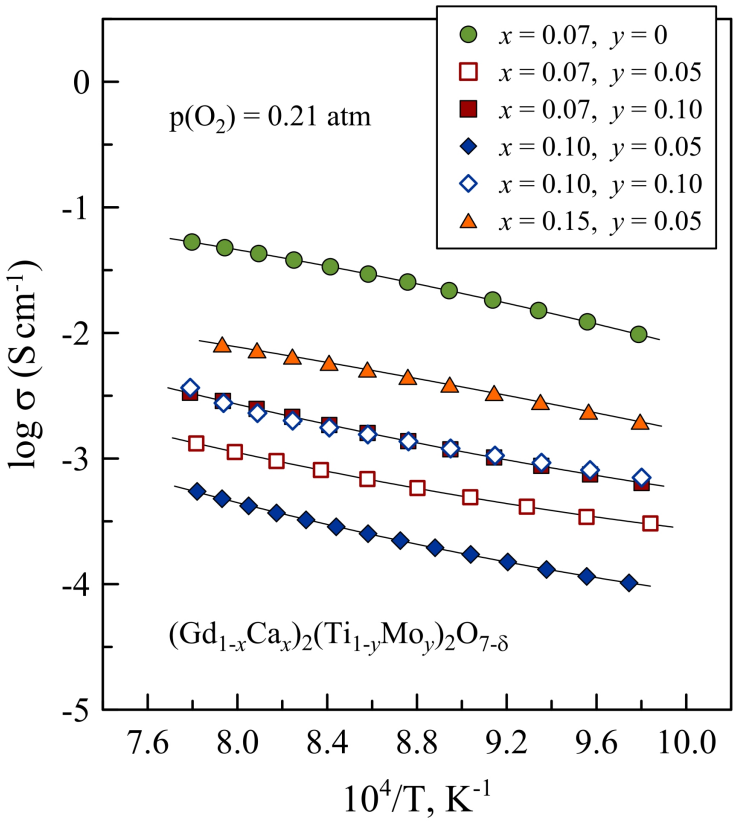

Fig. 22. Comparison of total (bulk + grain boundary) conductivity of $(Gd_{1-x}Ca_x)_2(Ti_{1-y}Mo_y)_2O_{7-\delta}$ ceramics in high-temperature range in air.

3.4.2. Bulk and grain boundary contributions

The results of impedance spectroscopy studies demonstrated that grain boundary contribution to the total resistivity can be neglected at T ≥ 650°C in the case of $(Gd_{0.93}Ca_{0.07})_2Ti_2O_{7-\delta}$ and above 750°C for $(Gd_{1-x}Ca_x)_2(Ti_{0.95}Mo_{0.05})_2O_{7-\delta}$ ceramics. At lower temperatures, grain boundary resistivity rapidly increases with cooling and becomes dominant in Mo substituted materials below 500–600°C. Examples of fitting of impedance spectra at low temperatures are presented on Fig. 23.

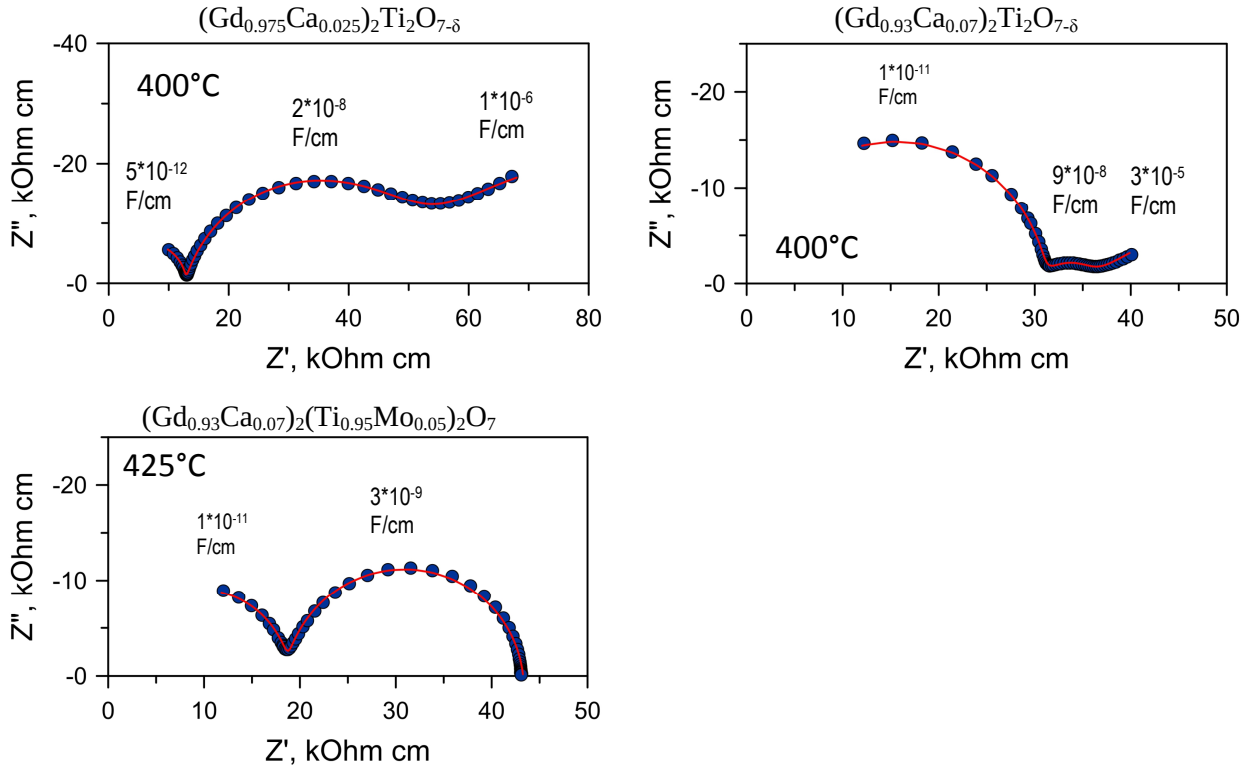

Fig. 23. Impedance spectra of $(Gd_{1-x}Ca_x)_2Ti_2O_{7-\delta}$ materials at lower temperatures in air.

Semicircles with capacitance values in a range ~10^{-11} –10^{-12} are attributed to bulk processes, and ~10^{-8} –10^{-11} to grain boundary (Table 3). Increase in level of calcium doping in $(Gd_{1-x}Ca_x)_2Ti_2O_{7-\delta}$ compositions increases contribution of grain bulk resistivity at low temperatures to the total resistivity and significantly reduces contribution of grain boundaries (Fig. 23).

Fig. 24 shows electrical conductivity of bulk of $(Gd_{1-x}Ca_x)_2Ti_2O_{7-\delta}$ and $(Gd_{1-x}Ca_x)_2(Ti_{0.95}Mo_{0.05})_2O_{7-\delta}$ in air. In the case of doping only by calcium, there are opposite correlations between conductivity and doping level in high-temperature and low-temperature regions. This phenomenon can be explained by defects association at lower temperatures:

$$V_O^{\bullet\bullet} + Ca'_{Gd} \leftrightarrow (V_O Ca_{Gd})^{\bullet}, \quad (14)$$

which reduces the mobility of oxygen ions . At the same time defect association leads to increase of activation energies resulting in change in slope of Arrhenius dependencies of electrical conductivity.

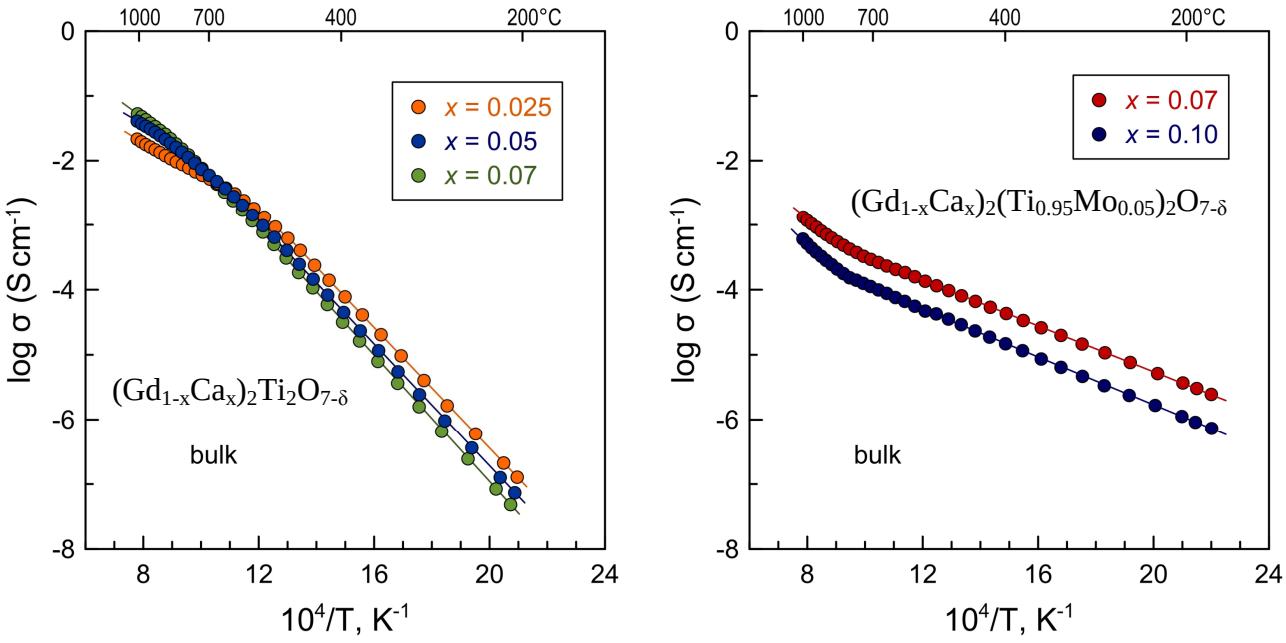

Fig. 24. Temperature dependence of bulk conductivity of $(Gd_{1-x}Ca_x)_2(Ti_{1-y}Mo_y)_2O_{7-\delta}$ ceramics in dry air.

3.4.3. Transference numbers and ionic conductivity

The average oxygen-ion transference numbers under air/oxygen gradient determined by the modified EMF technique are listed in Table 7. $(Gd_{0.93}Ca_{0.07})_2Ti_2O_{7-\delta}$ ceramics demonstrated comparatively high oxygen-ionic conductivity with minor (~3%) electronic contribution to total electrical transport, in excellent agreement with previous reports [2].

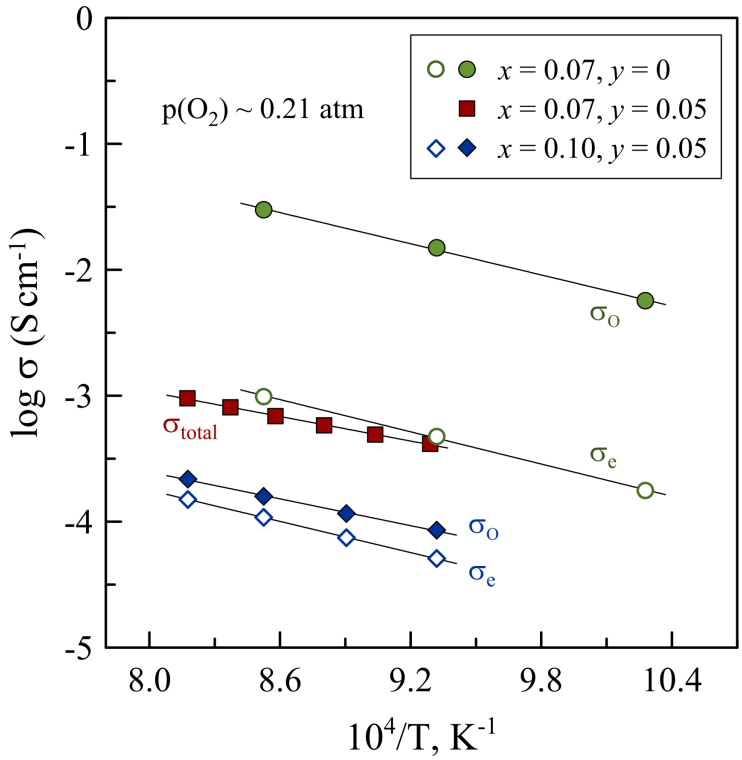

Fig. 25. Temperature dependence of partial oxygen-ionic (σ_O) and electronic (σ_e) conductivities of $(Gd_{1-x}Ca_x)_2(Ti_{1-y}Mo_y)_2O_{7-\delta}$ ceramics estimated from the data on total conductivity in air and average transference numbers under O_2/air gradient. Note that, for $((Gd_{0.93}Ca_{0.07})_2(Ti_{0.95}Mo_{0.05})_2O_{7-\delta}$, $\sigma_{total} \approx \sigma_e$ and σ_O ~10^{-6} to 10^{-5} S/cm at 950°C.

The ion transference numbers under oxygen/air gradient of $(Gd_{0.93}Ca_{0.07})_2(Ti_{0.95}Mo_{0.05})_2O_{7-\delta}$ decrease to values below the experimental error of the EMF technique: the ratio between observed and theoretical EMF was ~0.001 at 950°C and decreased on cooling (Table 7). $(Gd_{0.90}Ca_{0.10})_2(Ti_{0.95}Mo_{0.05})_2O_{7-\delta}$ ceramics demonstrated even lower conductivity, but much higher oxygen-ion transference number (0.59–0.67) at 700–950°C. These differences are summarized in Fig. 25, which shows temperature dependencies of partial ionic and electronic conductivities estimated from the total conductivity in air and average transference numbers under O_2/air gradient. The determined transference numbers relate to the total (grain interior and boundaries) electrical transport; therefore, the values of partial conductivities for Mo-substituted ceramics are shown only for T ≥800°C.

Table 7. Average oxygen-ion transference numbers of $(Gd_{1-x}Ca_x)_2(Ti_{1-y}Mo_y)_2O_{7-\delta}$ ceramics determined by modified EMF technique.($p(O_2)$in Argon flow was $5\cdot10^{-5}$ atm; $p(O_2)$ in 10% H_2–N_2 flow corresponded to $2\cdot10^{-20}$ atm at 900°C

Composition	**T°C**	**Average t_O under oxygen partial pressure gradient**		
		O_2/Air	**Air/Argon**	**Air/10% H_2-N_2**
x =0.025, y = 0	900	0.923	-	0.978
	800	0.921	-	0.988
	700	0.914	-	0.994
x =0.05, y = 0	900	0.973	-	0.993
	800	0.966	-	0.997
	700	0.970	-	0.999
x =0.07, y = 0	900	0.968	-	0.991
	800	0.969	-	0.998
	700	0.970	-	0.998
x = 0.07, y = 0.05	950	$E_{obs}/E_{theor} \leq 0.001$	$E_{obs}/E_{theor} \leq 0.001$	0.406
	900			0.386
	850			0.368
	800			0.344
	750			0.331
	700			0.288
x = 0.10, y = 0.05	950	0.592	0.727	0.697
	900	0.595	0.750	0.674
	850	0.609	0.779	0.665
	800	0.627	0.808	0.685
	750	0.645	0.837	0.664
	700	0.672	0.863	0.700

Table 8. Activation energy of total and partial ionic and electronic conductivities of $(Gd_{1-x}Ca_x)_2(Ti_{1-y}Mo_y)_2O_{7-\delta}$ in air.

Composition	**Conductivity**	**T°C**	**E_a, kJ/mol**
x = 0.07, y = 0	σ_{total}	780–1010	77.1 ± 1.0
	σ_O	700–900	87.8 ± 3.0
	σ_e	700–900	90.5 ± 2.4
x = 0.07, y = 0.05	$\sigma_{total} \approx \sigma_e$	770–1010	73.6 ± 1.3
x = 0.10, y = 0.05	σ_{total}	780–1010	85.2 ± 1.6
	σ_O	800–950	77.4 ± 2.4
	σ_e	800–950	88.5 ± 0.8

3.5. Electrical conductivity as function of p(O_2)

Fig. 26 shows oxygen partial pressure dependence of electrical conductivity of $(Gd_{1-x}Ca_x)_2Ti_2O_{7-\delta}$ ceramics at 900°C. In agreement with the literature reports on $(Gd_{1-x}Ca_x)_2Ti_2O_{7-\delta}$ system [1, 31] and also according to the ion transport number (Table 7), Ca-substituted ceramics show a plateau-like behaviour over a wide range of oxygen partial pressure where ionic transport is dominant. The conductivity starts to increase under highly reducing conditions because of increasing oxygen-ionic and n-type electronic transport in accordance with reduction reaction:

$$O_O^{\times} \xleftrightarrow{k_{red}} V_O^{\bullet\bullet} + 2e' + 0.5O_2 \qquad (15)$$

In oxidizing atmospheres there is a minor p-type contribution:

$$0.5O_2 + V_O^{\bullet\bullet} \xrightarrow{ox} O_O^{\times} + 2h^{\bullet} \qquad (16)$$

Compositions with higher calcium doping level have less pronounced rise of p- and n-type conductivity under highly reducing and oxidizing conditions, respectively, due to higher concentration of oxygen vacancies and therefore higher ionic conductivity.

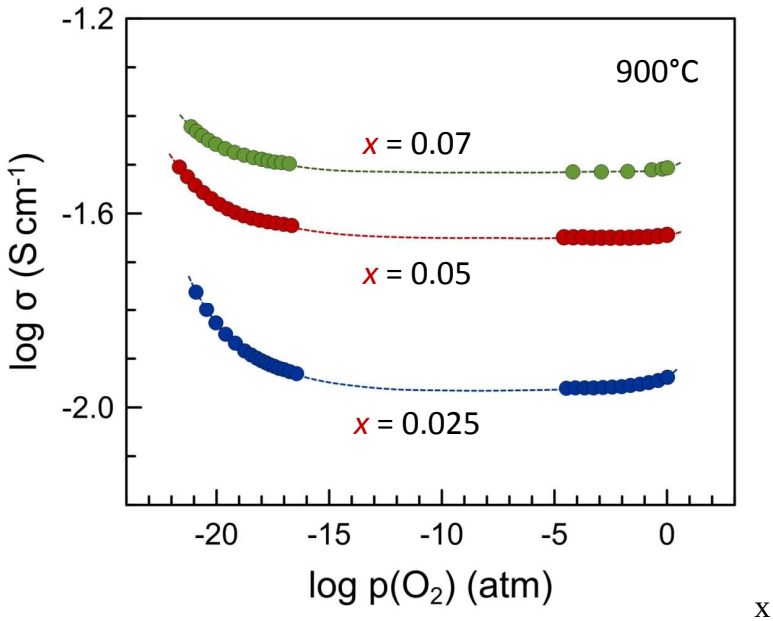

Fig. 26. Oxygen partial pressure dependence of electrical conductivity of $(Gd_{1-x}Ca_x)_2Ti_2O_{7-\delta}$ ceramics at 900°C. Dotted lines are guide for the eye.

Behavior of σ vs. p(O_2) for co-substituted $(Gd_{1-x}Ca_x)_2(Ti_{0.95}Mo_{0.05})_2O_{7-\delta}$ ceramics is markedly different (Fig. 27). The shape of log σ–log $p(O_2)$ curves strongly depends on the dopant compensation mechanism. p(O_2)-dependence of electrical conductivity of $(Gd_{0.93}Ca_{0.07})_2(Ti_{0.95}Mo_{0.05})_2O_{7-\delta}$ has an electronic plateau under inert and oxidizing conditions

and rather unusual transition to mixed conduction under reducing conditions, as revealed by the average ion transport number (Table 7). The electronic plateau can be ascribed to hopping involving co-existence of Mo^{n+} ions of different oxidation states, such as the prevailing Mo^{4+}/Mo^{6+} pair proposed earlier [3] or Mo^{5+}/Mo^{6+} if one considers the evidence of 2-step changes in oxygen stoichiometry (Fig. 17 and Fig. 18). In fact, 2-electron hopping seems unusual in high-temperature mixed conductors, even if bipolaron have been considered in other materials such as conducting polymers [32] and superconductors [25].

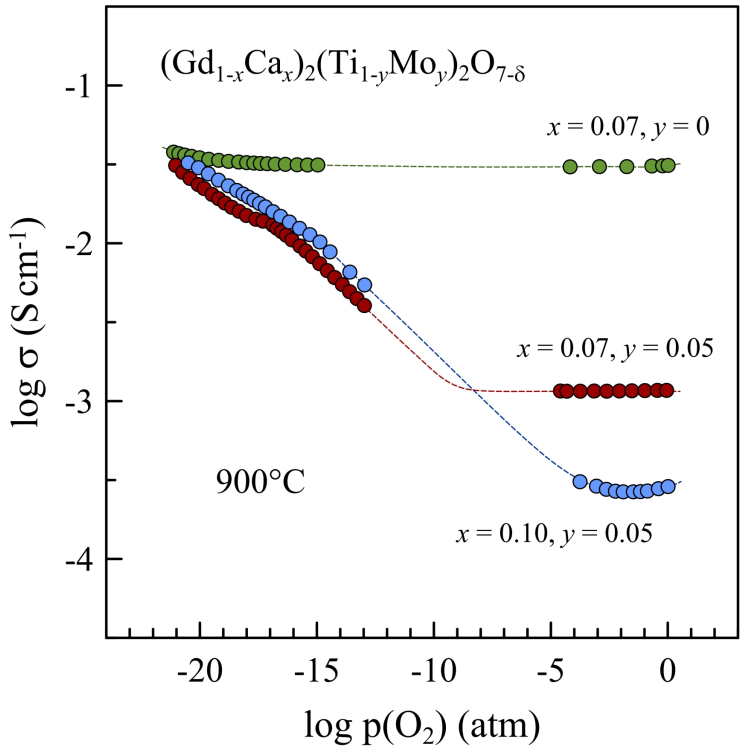

Fig. 27. Oxygen partial pressure dependence of electrical conductivity of $(Gd_{1-x}Ca_x)_2(Ti_{1-y}Mo_y)_2O_{7-\delta}$ ceramics at 900°C. Dotted lines are guide for the eye.

The electrical conductivity of mixed-conducting $(Gd_{0.90}Ca_{0.10})_2(Ti_{0.95}Mo_{0.05})_2O_{7-\delta}$ ceramics is also unusual, since its mixed conducting behavior is observed in the oxidizing region with $p(O_2) \sim 5\cdot10^{-3}$ to 10^{-1} atm, with a conductivity minimum characteristic of a state when $\sigma_n = \sigma_p$ and with slightly prevailing ionic transport. The latter is confirmed by increased average $t_o > 0.5$ under air/argon gradient (Table 7). In addition, one expects much higher mobility of electronic species μ_n, $\mu_p >> \mu_V$ as reported by others [22], implying even larger differences between the concentrations of ionic and electronic carriers, i.e.:

$$\sigma_i = q_i \cdot n_i \cdot \mu_i \Rightarrow \qquad [V_O^{\bullet\bullet}] \approx \frac{\sigma_V}{2e\mu_V} >> n \approx p \approx \frac{\sigma_n}{e\mu_n} \approx \frac{\sigma_p}{e\mu_p} \tag{17}$$

where the subscripts identify different ionic and electronic contributions to the total conductivity. Note also that one expects a prevailing ionic conductivity by vacancies, except possibly at very high temperatures, when the diffusivities of interstitial oxygen and vacancies converge to each other. Thus,

$$[V_O^{\bullet\bullet}][O_i''] = k_{aF} \approx [V_O^{\bullet\bullet}]^2 \approx [O_i'']^2 >> k_e = np \tag{18}$$

and the corresponding power law dependences for the concentrations of electrons and electron holes near the conductivity minimum can be predicted on combining this nearly constant concentration of ionic defects with the equilibrium constants of reactions of reduction and band-band transfer (electronic disorder):

$$O_O^{\times} \xleftrightarrow{k_{red}} V_O^{\bullet\bullet} + 2e' + 0.5O_2\,, \qquad k_{red} = [V_O^{\bullet\bullet}] \cdot n^2 \cdot p(O_2)^{1/2} \tag{19}$$

$$null \xleftrightarrow{k_e} e' + h^{\bullet}\,, \qquad k_e = np \tag{20}$$

$$O_O^{x} \xleftrightarrow{k_{aF}} V_O^{\bullet\bullet} + O_i''\,, \qquad k_{aF} = [V_O^{\bullet\bullet}][O_i''] \tag{21}$$

From eq. 18: $k_{aF} \approx [V_O^{\bullet\bullet}]^2 \Rightarrow [V_O^{\bullet\bullet}] \approx k_{aF}^{1/2}$

$$n = \frac{k_{red}^{1/2}}{[V_O^{\bullet\bullet}]^{1/2} p(O_2)^{1/4}} \approx \frac{k_{red}^{1/2}}{k_{aF}^{1/4}} p(O_2)^{-1/4} \tag{22}$$

$$p = \frac{k_e}{n} \approx \frac{k_e k_{aF}^{1/4}}{k_{red}^{1/2}} p(O_2)^{1/4} \tag{23}$$

Actually, the activation energy of ionic conductivity (Table 8) seems to be close to the expected value for the temperature dependence of mobility, contradicting the assumption that the concentration of ionic carriers is controlled by formation of anti-Frenkel defects. Thus, it seems that ionic carriers in $(Gd_{0.90}Ca_{0.10})_2(Ti_{0.95}Mo_{0.05})_2O_{7-\delta}$ are still determined by an extrinsic mechanism, presumably by a slight excess of acceptor additive, as a result of incomplete oxidation to hexavalent Mo^{6+} possibly combined with minor molybdenum oxide losses at high sintering temperatures due to the high volatility of MoO_3 [33]. Note that this is specific of the hexavalent state, implying much lower losses by stabilizing lower valence states, as expected under reducing conditions. Thus, one may assume a nearly constant concentration of oxygen vacancies, determined by volatilization during sintering and the resulting effective balance between acceptor and donor species (possibly including also slight redistribution of Ca^{2+} ions into octahedral sites to maintain A : B cation ratio:

$$[V_O^{\bullet\bullet}]_{ef} = 0.5[Ca'_{Gd}] + [O_i''] - 0.5[Mo_{Ti}^{\bullet}] - [Mo_{Ti}^{\bullet\bullet}] \tag{24}$$

Under these circumstances:

$$n \approx \frac{k_{red}^{1/2}}{[V_O^{\bullet\bullet}]_{ef}^{1/2}} p(O_2)^{-1/4} \quad (25)$$

$$p = \frac{k_e}{n} \approx \frac{k_e [V_O^{\bullet\bullet}]_{ef}^{1/2}}{k_{red}^{1/2}} p(O_2)^{1/4} \quad (26)$$

Nevertheless, this still results in increase in p-type conductivity in the mixed-conducting $(Gd_{0.90}Ca_{0.10})_2(Ti_{0.95}Mo_{0.05})_2O_{7-\delta}$, onset of a minor p-type contribution in the ionic conducting composition $(Gd_{0.93}Ca_{0.07})_2Ti_2O_{7-\delta}$, and increase of both n-type electronic and oxygen-ionic conductivities under reducing conditions in all compositions. The $p(O_2)$ corresponding to the onset of the conductivity rise depends on donor and acceptor concentrations (and therefore on charge compensation mechanism and conductivity level in the plateau region). Note the increment of total conductivity of $(Gd_{1-x}Ca_x)_2Ti_2O_{7-\delta}$ ceramics at reduced oxygen pressures was attributed previously only to increasing electronic contribution assuming $p(O_2)$-independent ionic conductivity [1, 31]. The results of this work demonstrate that this is not correct for $(Gd_{0.93}Ca_{0.07})_2Ti_2O_{7-\delta}$, as reflected by higher average t_O under air/10% H_2–N_2 gradients when compared to transference numbers under oxidizing conditions (Table 7). Co-substituted $(Gd_{1-x}Ca_x)_2(Ti_{0.95}Mo_{0.05})_2O_{7-\delta}$ (x = 0.07–0.10) ceramics are both mixed ionic-electronic conductors at reduced oxygen partial pressure (Table 7), but exhibit lower total electrical conductivity compared to Mo-free composition at intermediate oxygen partial pressures (Fig. 27), corresponding to fuel electrodes under significant fuel conversion or anodic overpotentials.

Under strongly reducing conditions with $p(O_2) \sim 10^{-21}$ atm at 900°C, all materials show comparable total electrical conductivity (Fig. 28), although $(Gd_{0.93}Ca_{0.07})_2Ti_2O_{7-\delta}$ is prevailing ionic conductor, and Mo-containing ceramics are mixed-conducting oxides. Semiconducting behavior indicates that concentrations of Ti^{3+} and Mo^{4+} are still too low to form a broad conduction band leading to metallic conductivity, and instead electronic transport occurs by electron hopping via Ti^{4+}/Ti^{3+} and Mo^{5+}/Mo^{4+} pairs. As in air, Arrhenius dependencies of electrical conductivity of Mo-substituted ceramics tend to lower activation energy on cooling.

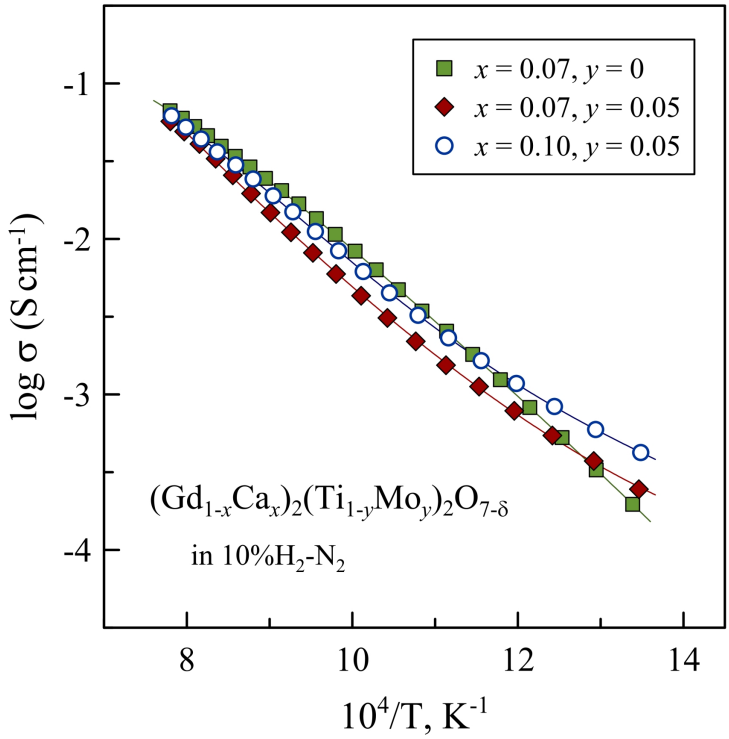

Fig. 28. Temperature dependence of electrical conductivity of $(Gd_{1-x}Ca_x)_2(Ti_{1-y}Mo_y)_2O_{7-\delta}$ ceramics in 10% H_2–N_2 atmosphere; ($p(O_2) \sim 3\cdot10^{-21}$ atm at 900°C).

3.6. Defect chemistry of Mo-doped $(Gd,Ca)_2Ti_2O_{7\pm\delta}$

A defect chemistry model is developed to support the analysis of transport properties; this analysis and method of solving are based on the expected reactions of anti-Frenkel disorder (eqn. (21)), reduction (eqn. (19)), band–band transfer (eqn. (20)), and valence changes of molybdenum ions, described as follows, to emphasize correlations between concentration of ionic charge carriers and polaron hoping between molybdenum cations with different valence states:

$$Mo_{Ti}^{\bullet\bullet} + 0.5O_O^{\times} \xleftrightarrow{k_1} Mo_{Ti}^{\bullet} + 0.25O_2 + 0.5V_O^{\bullet\bullet} \qquad k_1 = \frac{[Mo_{Ti}^{\bullet}][V_O^{\bullet\bullet}]^{1/2} pO_2^{1/4}}{[Mo_{Ti}^{\bullet\bullet}]} \qquad (27)$$

$$Mo_{Ti}^{\bullet} + 0.5O_O^{\times} \xleftrightarrow{k_0} Mo_{Ti}^{\times} + 0.25O_2 + 0.5V_O^{\bullet\bullet} \qquad k_0 = \frac{[Mo_{Ti}^{\times}][V_O^{\bullet\bullet}]^{1/2} pO_2^{1/4}}{[Mo_{Ti}^{\bullet}]} \qquad (28)$$

In order to establish correlations between transport properties and defect chemistry, one estimated the mobility of oxygen vacancies from the ionic conductivity plateau of composition $(Gd_{0.93}Ca_{0.07})_2Ti_2O_{7-\delta}$; $\mu_V = \sigma_o / \left(e \cdot [Ca'_{Gd}]\right) \approx 3.6\cdot10^{-4}$ $cm^2V^{-1}s^{-1}$. Differences relative to other reported results [22] may be related to contents of aliovalent additives, with expected impact on defect interactions and mobility. The n-type contribution in this composition was also evaluated from the average ionic transport numbers under air/H_2 gradient; this was combined with eqn (25)

and a typical value of electron mobility $\mu_n \approx 0.014$ $cm^2V^{-1}s^{-1}$ at 900°C [34] to evaluate the order of magnitude of the equilibrium constant of the reduction reaction (eqn (19)) $k_{red} \approx 10^{47}$ $cm^{-9}atm^{1/2}$. Indeed, this depends on the assumed value of mobility and vice versa. Corresponding results for the p-type conductivity were also evaluated by transport number measurements under O_2/air gradients and used to estimate the mobility of holes for a typical value of equilibrium constant of band–band transfer $k_e \approx 2.9\ 10^{30}$ cm^{-6} [35], combined with the actual value of k_{red}; this also yields mp $\mu_p \approx 0.014$ $cm^2V^{-1}s^{-1}$. One also assumed a typical value of equilibrium constant for anti-Frenkel disorder $k_{aF} \approx 2.8 \cdot 10^{27}$ cm^{-6} taken from ref. 35.

The parameters estimated for composition $(Gd_{0.93}Ca_{0.07})_2Ti_2O_{7-\delta}$ were then used to predict a defect chemistry model for composition $(Gd_{0.93}Ca_{0.07})_2(Ti_{0.95}Mo_{0.05})_2O_{7-\delta}$, based also on the measured dependence of total conductivity and transport number; this is shown in Fig. 29. The model includes polaron hopping, assuming that this may comprise single-electron hopping between pairs $Mo_{Ti}^{\bullet} / Mo_{Ti}^{\bullet\bullet}$ and $Mo_{Ti}^{\times} / Mo_{Ti}^{\bullet}$ with similar mobilities, i.e.:

$$\sigma_{pol} = e\mu_{pol} \frac{[Mo_{Ti}^{\bullet\bullet}][Mo_{Ti}^{\bullet}] + [Mo_{Ti}^{\bullet}][Mo_{Ti}^{\times}]}{[Mo_{Ti}]_{total}} \qquad (29)$$

The actual fitting reproduces quite well the measured transport properties and indicates that the prevailing hopping contribution involves the $Mo_{Ti}^{\bullet} / Mo_{Ti}^{\bullet\bullet}$ pair rather than $Mo_{Ti}^{\times} / Mo_{Ti}^{\bullet}$, as given by corresponding equilibrium constants $k_1 >> k_0$. Note that this is needed to reach reasonable fitting for the average ion transport number. In addition, this is consistent with the changes in oxygen stoichiometry upon exposition to reducing atmosphere (Fig. 18) with an initial fast evolution within the expected range for reduction of Mo^{6+} to Mo^{5+} and then lower (and slower) contribution of subsequent reduction to Mo^{4+}.

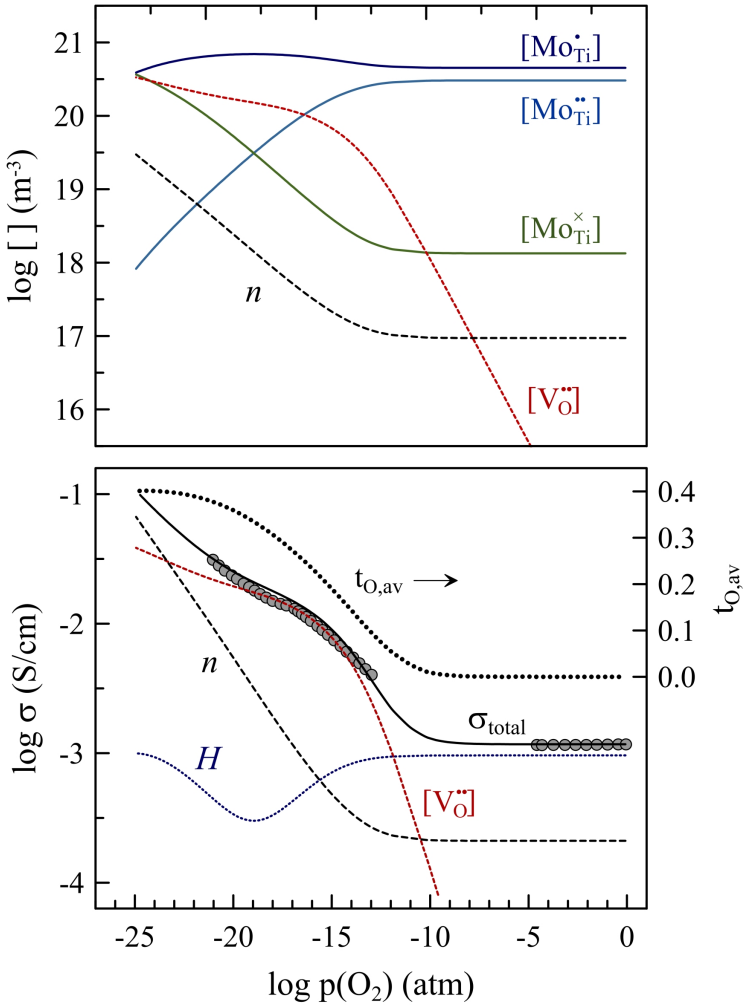

Fig. 29. Defect chemistry diagram of $(Gd_{0.93}Ca_{0.07})_2(Ti_{0.95}Mo_{0.05})_2O_{7-\delta}$ composition at 900°C (top) and corresponding fitting of transport properties (bottom). Experimental data are shown by circles. The average oxygen-ion transference number $t_{O,av}$ corresponds to air/$p(O_2)$ gradient.

One also obtained good fitting for the transport properties of the mixed conducting composition $(Gd_{0.90}Ca_{0.10})_2(Ti_{0.95}Mo_{0.05})_2O_{7-\delta}$ (Fig. 30). One expects however previous molybdenum oxide losses during sintering, as explained above. Then, the effective concentration of oxygen vacancies was estimated on combining the conductivity minimum with the ionic transport number under air/Ar gradient and mobility of vacancies; this also allowed one to re-assess the effective Mo contents. In addition, suitable fitting of the transport properties of this sample required significantly higher mobilities of electron holes and polarons and slightly lower mobility of vacancies (Table 9), to reproduce the measured dependence of conductivity on oxygen partial pressure and average values of ionic transport number. Lower equilibrium constants of reduction of Mo^{6+} to lower valence are also needed to attain good fitting, thus indicating lower reducibility of composition $(Gd_{0.90}Ca_{0.10})_2(Ti_{0.95}Mo_{0.05})_2O_{7-\delta}$ compared to $(Gd_{0.93}Ca_{0.07})_2(Ti_{0.95}Mo_{0.05})_2O_{7-\delta}$, as expected on increasing the concentration of the acceptor-type additive.

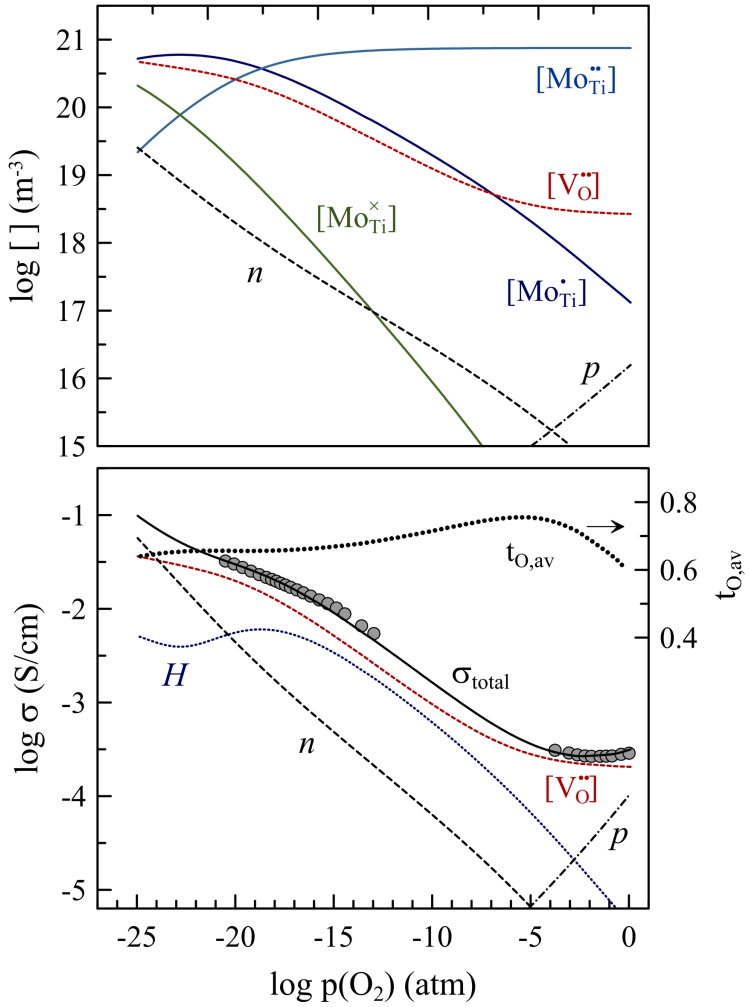

Fig. 30. Defect chemistry diagram of $(Gd_{0.90}Ca_{0.10})_2(Ti_{0.95}Mo_{0.05})_2O_{7-\delta}$ composition at 900°C (top) and corresponding fitting of transport properties (bottom). Experimental data are shown by circles. The average oxygen-ion transference number $t_{O,av}$ corresponds to air/$p(O_2)$ gradient.

Table 9. Relevant defect chemistry parameters $(Gd_{1-x}Ca_x)_2(Ti_{1-y}Mo_y)_2O_{7-\delta}$

	x=0.07, y=0	**x=0.07, y=0.05**	**x=0.10, y=0.05**
k_{aF}, cm^{-6}	$2.8\cdot10^{27}$	$2.8\cdot10^{27}$	$2.8\cdot10^{27}$
k_{red}, $cm^{-9}atm^{1/2}$	10^{47}	10^{47}	10^{47}
k_e, cm^{-6}	$2.9\cdot10^{30}$	$2.9\cdot10^{30}$	$2.9\cdot10^{30}$
k_0, $atm^{1/4}$	—	10^4	$5\cdot10^3$
k_1, $atm^{1/4}$	—	$5\cdot10^6$	$3\cdot10^5$
μ_n, $cm^2V^{-1}s^{-1}$	0.014	0.014	0.014
μ_p, $cm^2V^{-1}s^{-1}$	0.014	0.014	0.042
μ_V, $cm^2V^{-1}s^{-1}$	$3.6\cdot10^{-4}$	$3.6\cdot10^{-4}$	$2.4\cdot10^{-4}$
μ_H, $cm^2V^{-1}s^{-1}$	—	$3.3\cdot10^{-5}$	$2\cdot10^{-4}$

3.7. Protonic transport in $Gd_2Ti_2O_7$-based pyrochlores

Fig. 31 compares total conductivities of $(Gd_{1-x}Ca_x)_2(Ti_{1-y}Mo_y)_2O_{7-\delta}$ ceramics measured in dry and wet air at temperatures above 700ºC. The conductivity values remains unchanged in dry and humidified atmospheres, within the limits of experimental uncertainty. Thus, there is no evidence of protonic transport in the studied ceramic materials in the high-temperature range (700-1000°C).

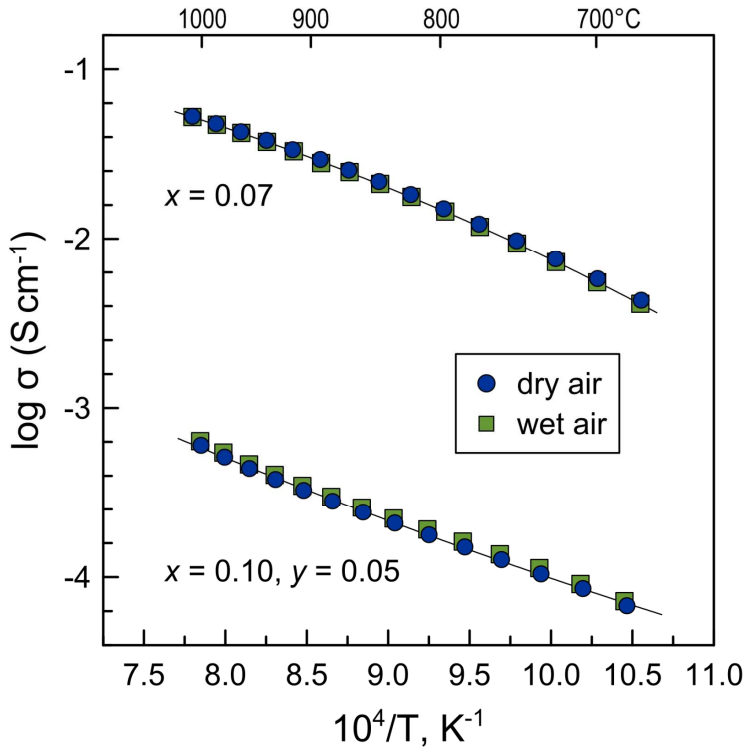

Fig. 31. Temperature dependence of electrical conductivity of $(Gd_{1-x}Ca_x)_2(Ti_{1-y}Mo_y)_2O_{7-\delta}$ in air. Dry air: $p(H_2O) < 10^{-3}$ atm; wet air $p(H_2O) \sim 0.03$ atm.

On the other hand, the results of impedance spectroscopy studies in the low-temperature range, when contribution of grain boundaries to the total resistivity becomes greater, provide clear evidence of the impact of humidity in the gas phase on transport properties of $Gd_2Ti_2O_7$-based pyrochlores. Furthermore, there is a correlation between variations of transport properties and oxygen vacancy concentration in the pyrochlore lattice, as shown below.

In the case of co-substituted titanates, $(Gd_{1-x}Ca_x)_2(Ti_{0.95}Mo_{0.05})_2O_{7-\delta}$ (x = 0.07-0.10), with negligible concentration of oxygen vacancies, humidity in the gas phase does not alter bulk resistivity, but decreases the resistivity of grain boundaries (Fig.32).

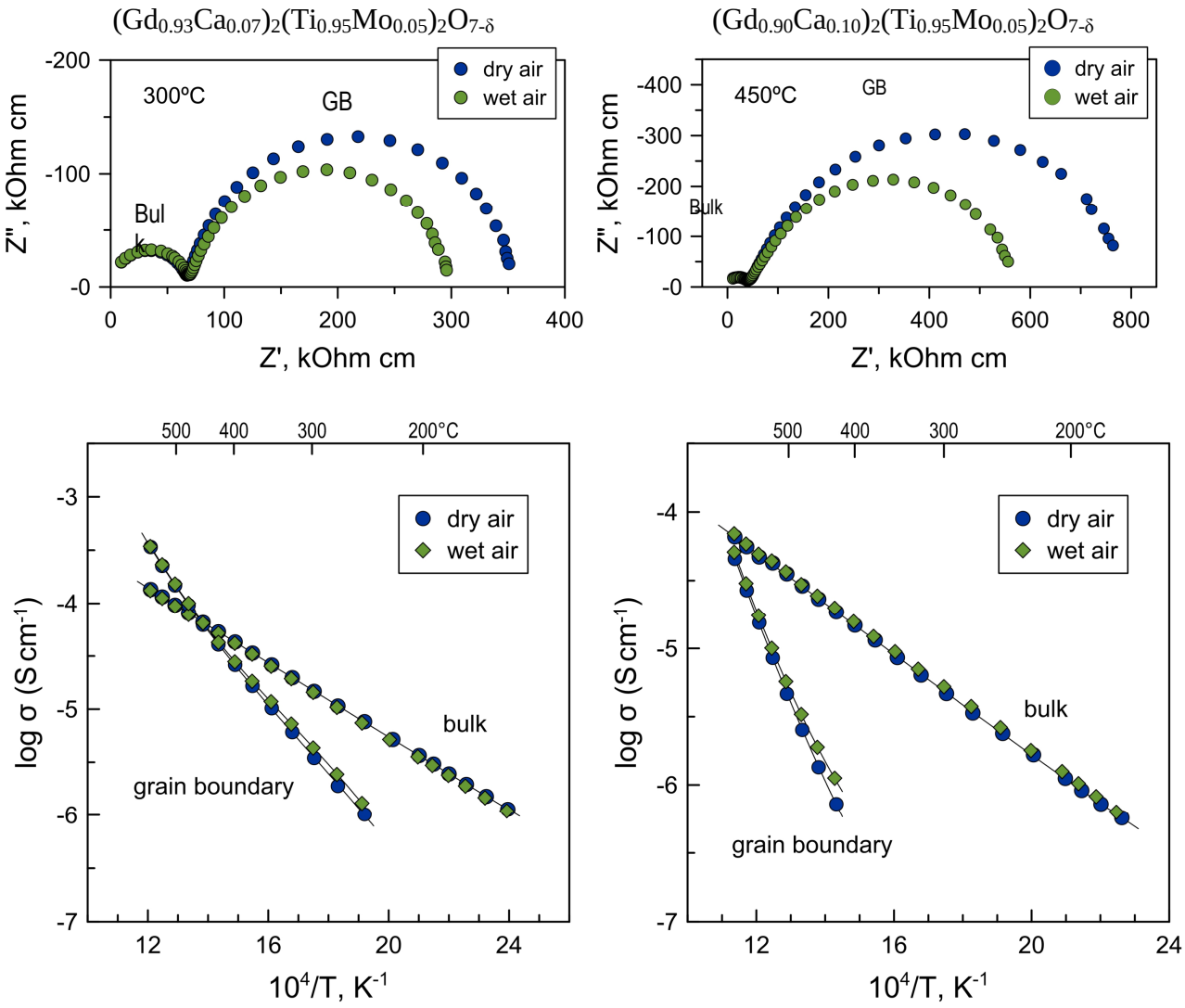

Fig. 32. Impedance spectra (top) and temperature dependencies of bulk and grain boundary conductivities (bottom) for $(Gd_{1-x}Ca_x)_2(Ti_{0.95}Mo_{0.05})_2O_{7-\delta}$ ceramics.

On the contrary, humidification of atmosphere decreases both bulk and grain boundary resistances in case of $(Gd_{1-x}Ca_x)_2Ti_2O_{7-\delta}$ ceramics. Impedance spectra and grain bulk and boundary conductivities of $(Gd_{0.975}Ca_{0.025})_2Ti_2O_{7-\delta}$ ceramics are presented in Fig. 33. The effect of humidity is clearly greater on the grain boundary resistivity compared to the bulk properties. While grain boundary conductivity increases in the entire analysed temperature range (≤ 600°C), the contribution of protonic transport to grain bulk conductivity becomes evident only at temperatures below ~400-450°C and increases on cooling.

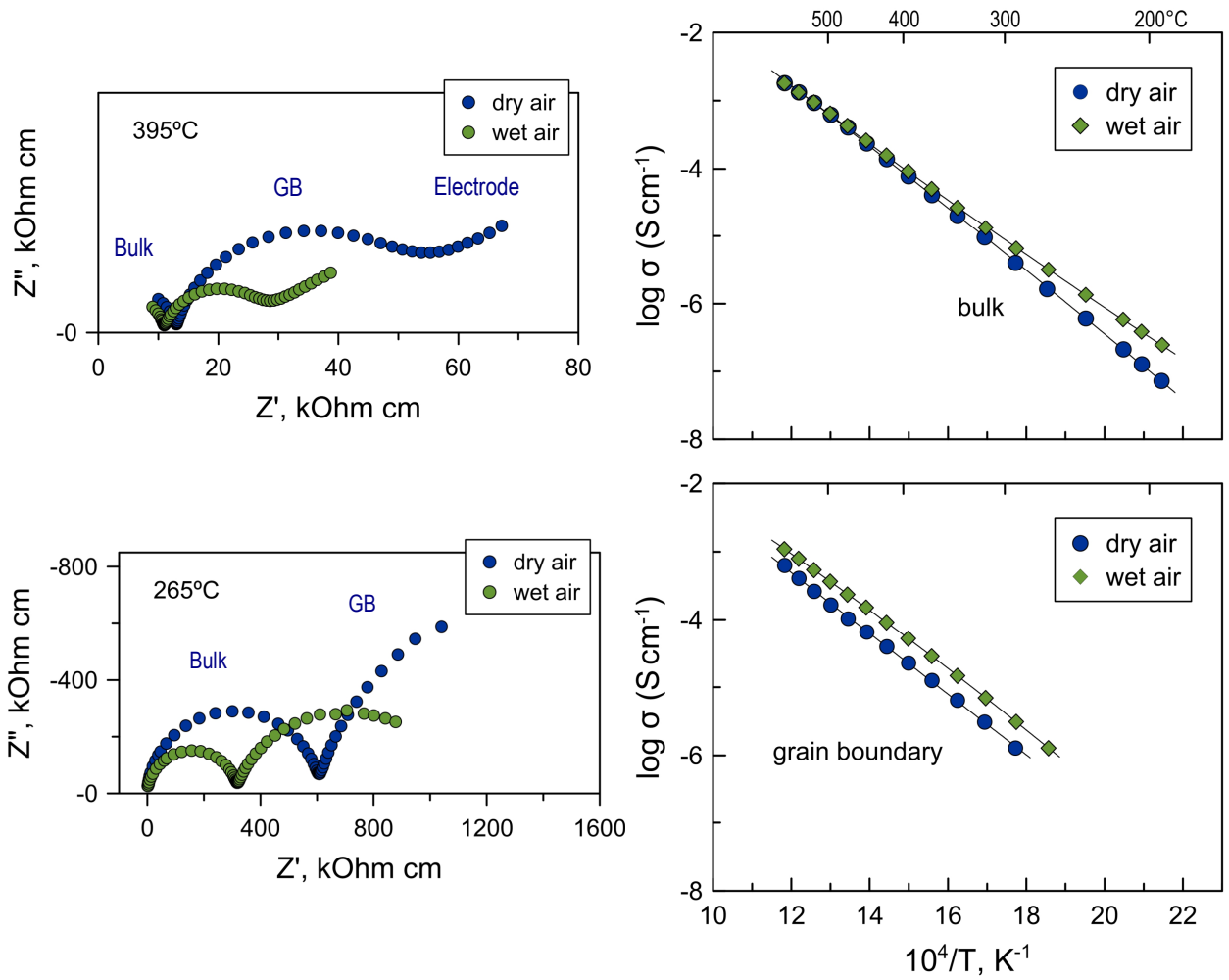

Fig. 33. Impedance spectra and temperature dependencies of bulk and grain boundary conductivity as function of temperature of $(Gd_{0.975}Ca_{0.025})_2Ti_2O_{7-\delta}$ ceramics.

Very similar results were obtained for other Ca-substituted compositions (Fig.34), although the impact of humidity on the grain boundary resistivity increases with increasing Ca contents (and therefore oxygen vacancy concentration). Grain boundary semicircle eventually disappears in low-temperature impedance spectra of $(Gd_{1-x}Ca_x)_2Ti_2O_{7-\delta}$ (x = 0.07) ceramics collected in wet air.

One may expect that protonic conductivity in $(Gd_{1-x}Ca_x)_2Ti_2O_{7-\delta}$ increases with concentration of oxygen vacancies due to hydration reaction:

$$H_2O + V_O^{\bullet\bullet} + O_O^x \leftrightarrow 2OH_O^{\bullet} \qquad (30)$$

and concentration of mobile protons should correlate with acceptor-doping level. Indeed, this seems to be confirmed, at least partly, by thermogravimetric analysis.

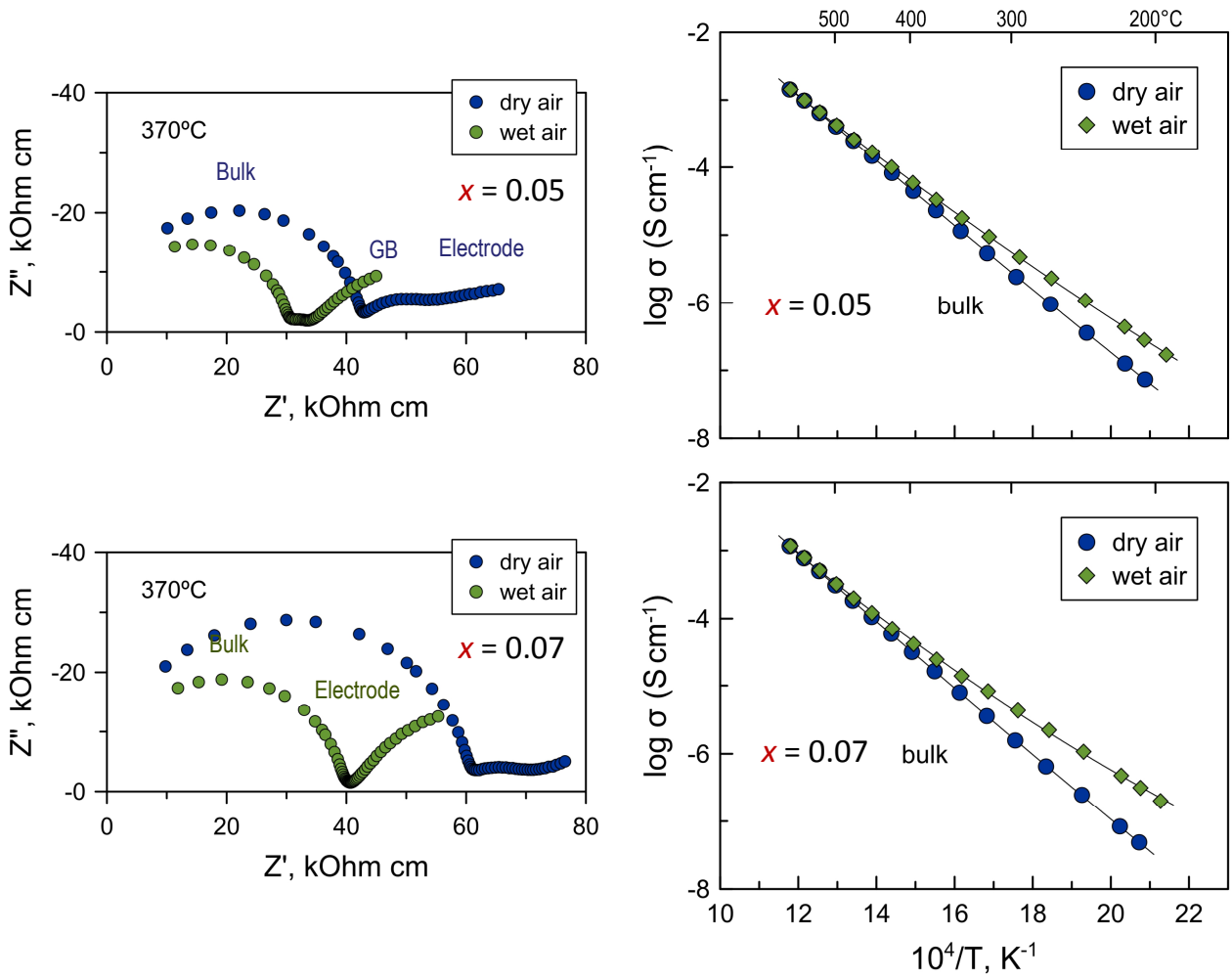

Fig. 34. Impedance spectra and temperature dependencies of bulk and grain boundary conductivity as function of temperature of $(Gd_{1-x}Ca_x)_2Ti_2O_{7-\delta}$ ceramics.

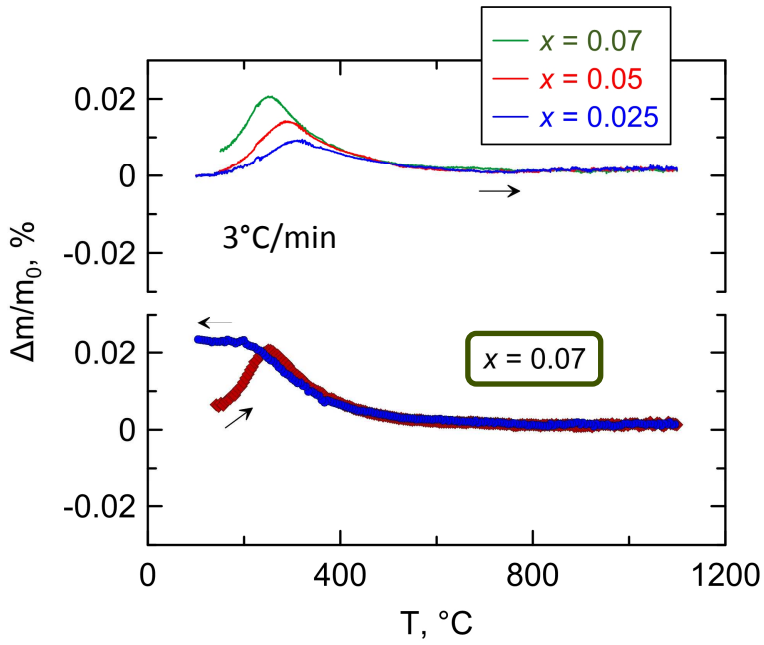

Fig. 35. Relative changes of mass of $(Gd_{1-x}Ca_x)_2Ti_2O_{7-\delta}$ ceramic samples on heating and cooling in wet N_2; $p(H_2O)$ ~ 0.015 atm. Powdered samples were preliminary calcined and cooled in dry N_2.

TGA was carried out to assess the water adsorption by $Gd_2Ti_2O_7$-based ceramics (Fig. 35). Water absorption on heating the powdered samples in humidified nitrogen was observed to reach a maximum at 250-320°C on heating and is reversible on cooling (Fig. 35). Although water uptake is relatively low, it correlates with the level of Ca-doping in $(Gd_{1-x}Ca_x)_2Ti_2O_{7-\delta}$. Estimations shows that, at peak of water absoption, the formula unit can be expressed as $(Gd_{0.93}Ca_{0.07})_2Ti_2O_{6.93}(H_2O)_{0.0055}$, i.e. oxygen content is much less than can be expected considering the concentration of oxygen vacancies.

Fig.36 shows temperature dependencies of bulk protonic conductivity calculated as a difference between conductivity in wet and in dry air. Estimated contribution of protonic conductivity is relatively high at low temperatures, with protonic transference numbers t_H close to ~ 0.5-0.075 at 250°C. Interestingly, the values protonic conductivity are almost independent of calcium content up to ~370°C (Fig. 36). In medium temperature range Bulk protonic conductivity reaches maximum at ~500°C and starts to drop at higher temperature, apparently due to water losses from the lattice.

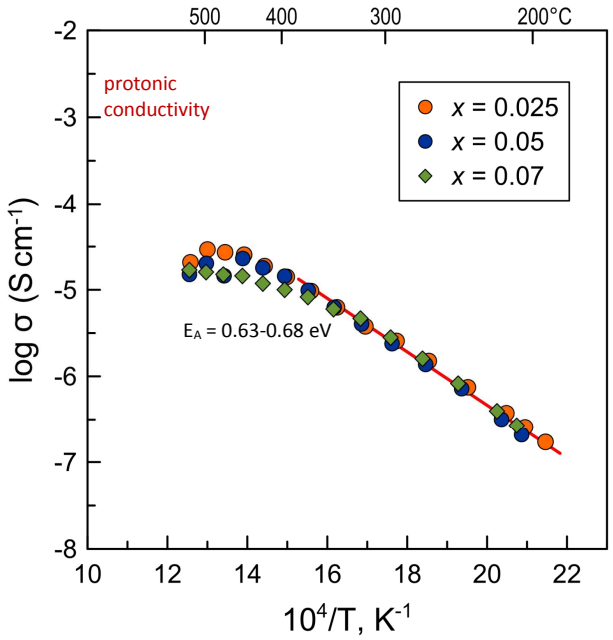

Fig. 36. Temperature dependence of protonic conductivity of $(Gd_{1-x}Ca_x)_2Ti_2O_{7-\delta}$ ceramics in low temperature range.

The values of bulk conductivity of $(Gd_{0.93}Ca_{0.07})_2Ti_2O_{7-\delta}$ ceramics measured at 400°C in wide range of oxygen partial pressure using dry and wet atmospheres shows some scatter if plotted vs $p(O_2)$ (Fig.37(top)). At the same time, the same values show nearly linear dependence if plotted vs water partial pressure (Fig.37(bottom)). This seem to indicate that electrical conductivity during isothermal measurements at lower temperatures is more affected by variations of $p(H_2O)$ rather than $p(O_2)$.

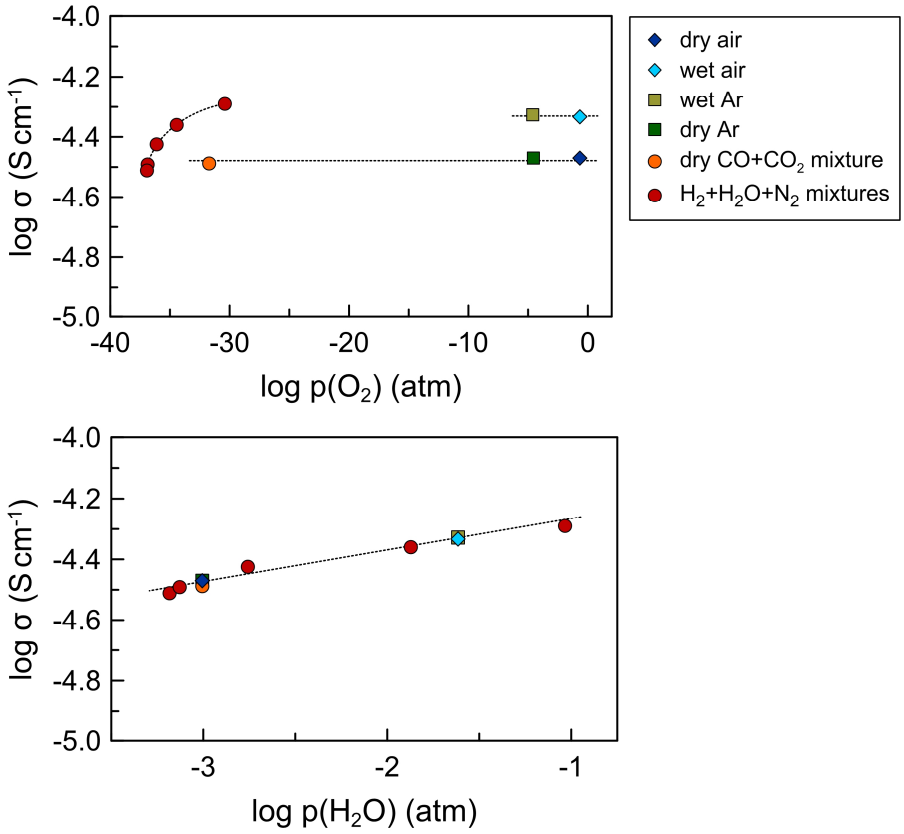

Fig.37. Bulk conductivity of $(Gd_{0.93}Ca_{0.07})_2Ti_2O_{7-\delta}$ ceramics measured at 400°C in different wet and dry atmospheres and plotted vs oxygen partial pressure (top) and vs water partial pressure (bottom).

3.8. Thermal expansion and dimensional stability

Pyrochlore-type $(Gd_{0.93}Ca_{0.07})_2Ti_2O_{7-\delta}$ ceramics demonstrate nearly linear dilatometric behavior in air at 25–1100°C and moderate average thermal expansion coefficients (TECs, Table 10) close to that of 8YSZ. Moderate substitution by molybdenum and minor variations of calcium content have rather negligible effect on the TEC values, albeit slightly improving linearity of expansion at higher temperatures (Fig. 38 and Table 10).

Table 10. Average thermal expansion coefficients of $(Gd_{1-x}Ca_x)_2(Ti_{1-y}Mo_y)_2O_{7-\delta}$ ceramics in air.

Composition	**T°C**	**($\alpha \times 10^{-6}$) ± 0.1, K^{-1}**
x = 0.07, y = 0	30–150	9.8
	150–800	10.4
	800–1100	11.3
	30–1100	10.6
x = 0.07, y = 0.05	30–150	9.9
	150–1100	10.8
	30–1100	10.7
x = 0.10, y = 0.05	30–150	9.5
	150–1100	10.6
	30–1100	10.5

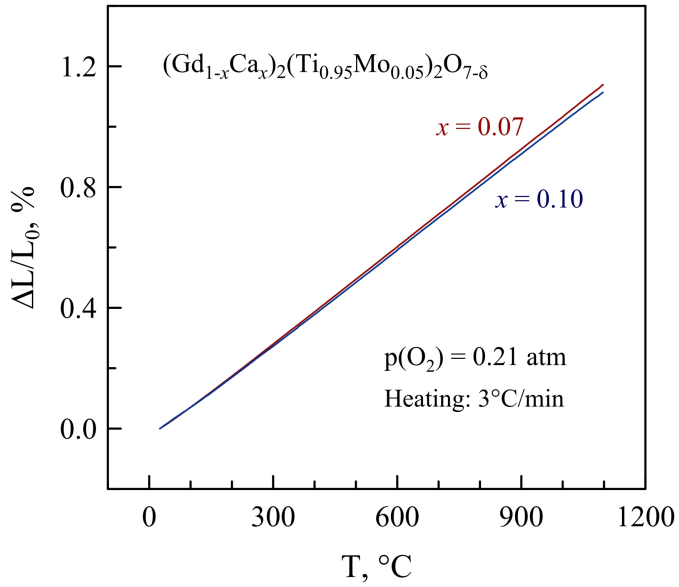

Fig. 38. Dilatometric curves of $(Gd_{1-x}Ca_x)_2(Ti_{0.95}Mo_{0.05})_2O_{7-\delta}$ ceramics in air.

Fig. 39 shows dimensional changes of $(Gd_{1-x}Ca_x)_2(Ti_{0.95}Mo_{0.05})_2O_{7-\delta}$ ceramics under isothermal conditions, on stepwise decrease of oxygen partial pressure from ambient to ~10^{-12} atm at 950°C. The data were collected after equilibration at each $p(O_2)$ for ~24 h. Literature data on some fluorite- and perovskite-type oxides are shown for comparison. Ceramic oxides containing variable valence cations often show dimensional changes on varying oxygen partial pressure at elevated temperatures. This phenomenon is usually referred to as chemical expansion or chemical strain and originates from two simultaneous competing processes occurring on reduction: (i) formation of oxygen vacancies leading to lattice contraction due to electrostatic

interactions, and (ii) simultaneous increase of cation radii causing lattice expansion due to steric effects. The latter contribution has a stronger impact, and oxygen losses at reduced $p(O_2)$ typically result in overall expansion of crystal lattice in the case of perovskite and fluorite structures (Fig. 39). In contrast, pyrochlore-type $(Gd_{1-x}Ca_x)_2(Ti_{0.95}Mo_{0.05})_2O_{7-\delta}$ ceramics demonstrate nearly zero dimensional changes in the studied $p(O_2)$ range despite oxygen losses on reduction. One may conclude that increasing oxygen deficiency under the studied conditions is associated mainly with reduction of molybdenum cations, while dimensional stability is provided by the pyrochlore-type titanate lattice. The low chemical expansion may be understood by taking into account that the ionic radii of Mo^{4+}, Mo^{5+} and Mo^{6+} in octahedral coordination only differ slightly [14]. The results of isothermal dilatometric studies are in agreement with negligible changes of room-temperature lattice parameters after reduction under even more reducing conditions (Table 4).

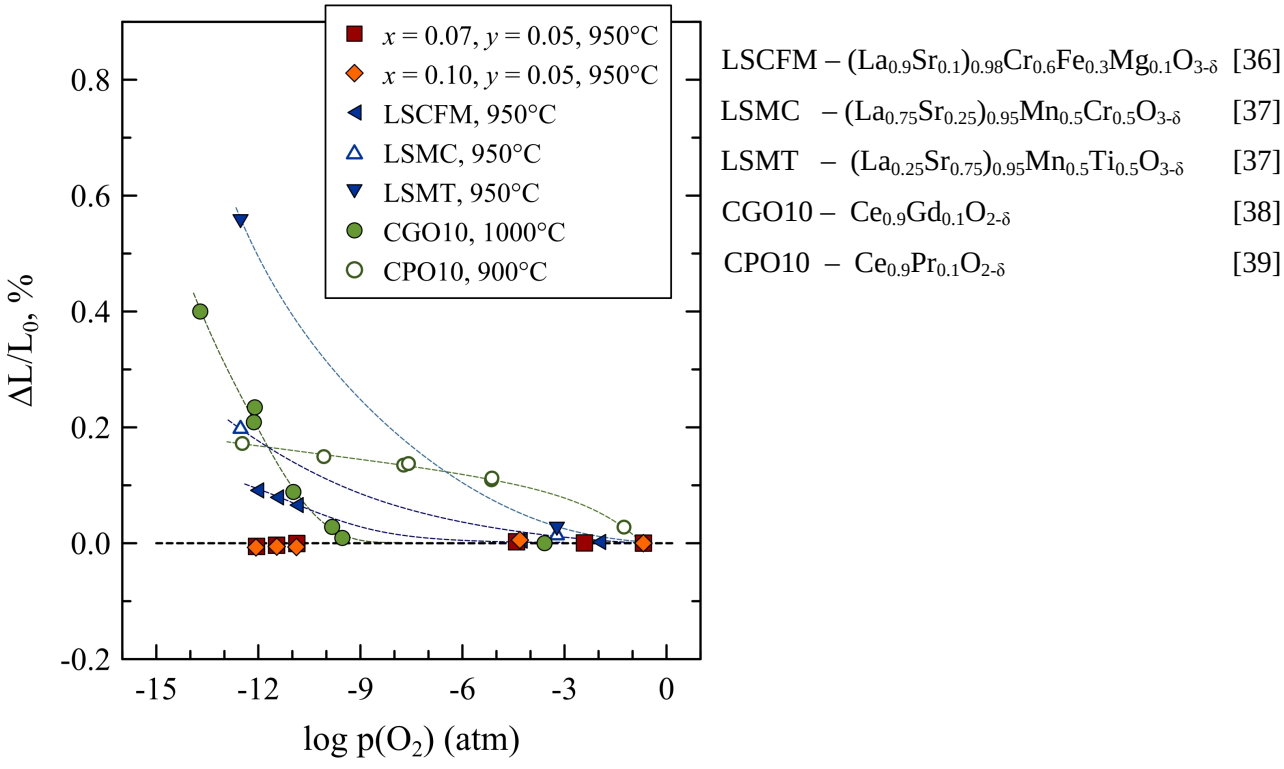

Fig. 39. Relative dimensional changes of $(Gd_{1-x}Ca_x)_2(Ti_{0.95}Mo_{0.05})_2O_{7-\delta}$ ceramics on reducing oxygen partial pressure at 950°C. Literature data on some perovskite- and fluorite-type oxides are shown for comparison. L_0 corresponds to the sample length at given temperature in air. Dotted lines are guide for the eye.

Conclusions

1. The domain of single-phase solid solutions with cubic pyrochlore-type structure in $(Gd_{1-x}Ca_x)_2(Ti_{1-y}Mo_y)_2O_{7\pm\delta}$ system is limited to $0.10 < x < 0.15$ and $0.05 < y < 0.10$ under oxidizing conditions;

2. $(Gd_{1-x}Ca_x)_2(Ti_{0.95}Mo_{0.05})_2O_{7-\delta}$ ceramics demonstrate good phase stability in a wide range of oxygen partial pressures: no degradation or phase decomposition was evidenced in the course of electrical and thermogravimetric studies and by subsequent XRD;

3. Dopant compensation mechanism and type of dominating charge carriers under oxidizing conditions strongly depend on calcium/molybdenum ratio. Electrical conductivity decreases with Mo substitution and changes from predominantly oxygen-ionic in $(Gd_{0.93}Ca_{0.07})_2Ti_2O_{7-\delta}$ to predominantly electronic in $(Gd_{0.93}Ca_{0.07})_2(Ti_{0.95}Mo_{0.05})_2O_{7-\delta}$ and to mixed ionic-electronic in $(Gd_{0.90}Ca_{0.10})_2(Ti_{0.95}Mo_{0.05})_2O_{7-\delta}$;

4. Reducing oxygen partial pressure increases both ionic and n-type electronic conductivities in substituted $Gd_2Ti_2O_7$ ceramics. $(Gd_{1-x}Ca_x)_2(Ti_{1-y}Mo_y)_2O_{7-\delta}$ ceramics exhibit mixed conductivity under SOFC anode operation conditions, which is however lower compared to $(Gd_{0.93}Ca_{0.07})_2Ti_2O_{7-\delta}$ and rather too low for electrode applications, except possibly to enhance electrocatalytic activity;

5. $Gd_2Ti_2O_7$-based pyrochlores show no detectable protonic transport at elevated temperatures (700-1000°C). In low temperature range, protonic transport in grains bulk and along the grain boundaries correlate with concentration of oxygen vacancies, with stronger impact of humidity on the grain boundary resistivity. Protonic contribution to the bulk conductivity of Ca-substituted gadolinium titanate reaches 50-75% at 250°C.

6. Co-substituted ceramics show moderate thermal expansion coefficients similar to that of 8YSZ, and remarkable dimensional stability on variations of oxygen partial pressure at 950°C.

List of references:

1. S.A. Kramer, H.L. Tuller, Solid State Ionics, 1995, 82, 15.
2. V.V. Kharton, E.V. Tsipis, A.A. Yaremchenko, N.P. Vyshatko, A.L. Shaula, E.N. Naumovich, J.R. Frade, Journal of Solid State Electrochemistry, 2003, 7(8), 468.
3. O. Porat, C. Heremans, H.L. Tuller, Solid State Ionics, 1997, 94, 75.
4. K. Huang, J. B. Goodenough, Solid Oxide Fuel Cell Technology: Principles, Performance and Operations, Woodhead Publishing, 2009, p. 340.
5. P. Holtappels, F. W. Poulsen and M. Mogensen, Solid State Ionics, 2000, 135, 675.
6. C. C. Barry, N. M. Grant, Ceramic Materials - Science and Engineering, Springer-Verlag New York 2013.
7. I. Pilatowsky, R.J. Romero, C.A. Isaza, S.A. Gamboa, P.J. Sebastian, W. Rivera, Cogeneration Fuel Cell-Sorption Air Conditioning Systems, 2011, 160p.
8. T.L. Cable, J. A. Setlock, International Journal of Applied Ceramic Technology, 2011, 8 (1), 1.
9. T. Chen, W.G. Wang, H. Miao, T. Li, C. Xu, Journal of Power Sources, 2011, 196, 2461.
10. Y.H. Heo, J.W. Lee, S.B. Lee, T.H. Lim, S.J. Park, R.H. Song, C.O. Park, D.R. Shin, Int. Journal of Hydrogen Energy, 2011, 36, 797.
11. L. Cai, A.L. Arias, J.C. Nino, J. Mater. Chem., 2011, 21, 3611.
12. J. S. Gardner, M. J. P. Gingras, J. E. Greedan, Reviews of Modern Physics, 2010, 82, 53.
13. T. Omata, S. Otsuka-Yao-Matsuo, Journal of the Electrochemical Society, 2001, 148(12), E475.
14. R. D. Shannon, Acta Crystallographica Section A, 1976, A32, 751.
15. V.V. Kharton, F.M.B. Marques, A. Atkinson, Solid State Ionics, 2004, 174, 135.
16. P. Holtappels, F. W. Poulsen and M. Mogensen, Solid State Ionics, 2000, 135, 675.
17. J. T. S. Irvine, D. C. Sinclair, A. R. West, Advanced materials, 1990, 2 (3), 132.
18. D. C. Sinclair, Boletín de la Sociedad Española de Cerámica y Vidrio, 1995, 34 (2), 55.
19. V.V. Kharton, F.M.B. Marques, Solid State Ionics, 2001, 140, 381.
20. M.J. Pascual, V.V. Kharton, E. Tsipis, A.A. Yaremchenko, C. Lara, A. Durán, J.R. Frade, Journal of the European Ceramic Society, 2006, 26, 3315.
21. A.A. Yaremchenko, V.V. Kharton, E.N. Naumovich, F.M.B. Marques, J. of Electroceramics, 2000, 4(1), 233.
22. J. J. Sprague, PhD thesis, Massachusetts Institute of Technology, 1999.
23. J. G. Choi, L. T. Thompson, Applied Surface Science, 1996, 93, 143.

24. S. Zador, C. B. Alcock, The Journal of Chemical Thermodynamics, 1970, 2, 9.

25. A. S. Alexandrov, N. F. Mott, Reports on Progress in Physics, 1994, 57, 1197.

26. L. G. Shcherbakova, J. C. C. Abrantes, D. A. Belova, E. A. Nesterova, O. K. Karyagina and A. V. Shlyakhtina, Solid State Ionics, 2014, 261, 131.

27. J. B. Goodenough, Annual Review of Materials Research, 2003, 33, 91.

28. P. K. Moon and H. L. Tuller, Science and Technology of Fast Ion Conductors (NATO ASI series, Vol. 199), ed. H. L. Tuller and M. Balkanski, Plenum Press, New York, 1989, pp. 307–312.

29. J. W. Stevenson, T. R. Armstrong, D. E. McCready, L. R. Pederson, W. J. Weber, Journal of the Electrochemical Society, 1997, 144, 3613.

30. I. Kosacki, S. Kramer, H. L. Tuller, Solid State Phenomena, 1994, 39–40, 117.

31. S.A. Kramer, PhD thesis, Massachusetts Institute of Technology, 1994.

32. S.A. Brazovskii, N.N. Kirova, JETP Lett., 1981, 33,4.

33. L. Brewer, R.H. Lamoreaux, Bulletin of Alloy Phase Diagrams, 1980, 1, 85.

34. M. Spears, S. Kramer, P.K. Moon, H.L. Tuller, Materials Research Society Symposium Proceedings, 1991, 210, 703.

35. M.A. Spears, H.L. Tuller, Materials Research Society Symposium Proceedings, 1995, 369, 271.

36. A.A. Yaremchenko, V.V. Kharton, V.A. Kolotygin, M.V. Patrakeev, E.V. Tsipis, J.C. Waerenborgh, Journal of Power Sources, 2014, 249, 483.

37. V.A. Kolotygin, E.V. Tsipis, A.L. Shaula, E.N. Naumovich, J.R. Frade, S.I. Bredikhin, V.V. Kharton, Journal of Solid State Electrochemistry, 2011, 15, 313.

38. I. Yasuda, M. Hishinuma, Proceedings of the Third International Symposium Ionic and Mixed Conducting Ceramics (Electrochem. Soc. Proc. Vol. 97–24), ed. T. A. Ramanarayanan, Electrochem. Soc., Pennington, NJ, 1998, pp. 178–187.

39. S.R. Bishop, H.L. Tuller, Y. Kurua, B. Yildiz, Journal of the European Ceramic Society, 2011, 31, 2351.